

UILIAN DA ROCHA ALBINO

The climatic effects on infiltration and stability of geotextile reinforced walls

São Paulo  
2018



UILIAN DA ROCHA ALBINO

The climatic effects on infiltration and stability of geotextile reinforced walls

Dissertation presented to the Graduate Program in Civil Engineering at the Polytechnic School of the University of São Paulo to obtain the degree of Master of Science

Concentration area:  
Geotechnical Engineering

Advisors:  
Prof. Dr. Marcos Massao Futai  
Prof. Dr. Fernando H. M. Portelinha

São Paulo  
2018

Autorizo a reprodução e divulgação total ou parcial deste trabalho, por qualquer meio convencional ou eletrônico, para fins de estudo e pesquisa, desde que citada a fonte.

Este exemplar foi revisado e corrigido em relação à versão original, sob responsabilidade única do autor e com a anuência de seu orientador.

São Paulo, 04 de Novembro de 2018

Assinatura do autor: Uilian da Rocha Albino

Assinatura do orientador: Paulo Henrique Furtado

#### Catálogo-na-publicação

Albino, Uilian da Rocha

The climatic effects on infiltration and stability of geotextile reinforced walls / U. R. Albino -- versão corr. -- São Paulo, 2018.

99 p.

Dissertação (Mestrado) - Escola Politécnica da Universidade de São Paulo. Departamento de Engenharia de Estruturas e Geotécnica.

1.Nonwoven geotextile 2.Reinforced soil wall 3.Climate analyses  
4.Infiltration 5.Capillary barrier I.Universidade de São Paulo. Escola Politécnica. Departamento de Engenharia de Estruturas e Geotécnica II.t.

Dedico este trabalho aos meus pais.



## **ACKNOWLEDGMENTS**

I would like to express my most sincere gratitude to my dissertation advisor, Professor Marcos Massao Futai, for his dedicated support and guidance throughout the course of my study. I would also like to thank Professor Futai for the professional lessons and enthusiasm throughout the elaboration of this dissertation.

I would like to thank my co-advisor, Professor Fernando H. M. Portelinha, for his direction since the beginning of the academic activities, and for the support and suggestions during the development of this study.

I am grateful to my family, especially my parents Valmir Meneses Albino and Maria Alves da Rocha, who have always encouraged me on this journey and supported my decisions. I also thank my girlfriend/fiancée, Tássia Brito Andrade, for her support and affection during this journey.

I would like to take this opportunity to express my gratitude to all of the faculty members of the Civil Engineering Graduate Program at the Polytechnic School of the University of São Paulo. Thank you for all the knowledge transmitted and professional lessons.

A special thanks to the group GeoInfraUSP for receiving me with arms wide open and for their hospitality during this stage of my life.

Last but not least, thanks to all my graduate colleagues for the friendship and knowledge shared during these years.



## **AGRADECIMENTOS**

Ao meu orientador, Prof. Dr. Marcos Massao Futai, pela orientação, pela dedicação e suporte necessário para o desenvolvimento desse trabalho. Agradeço também pelas lições profissionais e pelo positivismo transmitido durante toda a elaboração dessa dissertação.

Ao meu coorientador, Prof. Dr. Fernando Henrique Martins Portelina, pela coorientação desde o início das atividades acadêmicas, pelo apoio e sugestões durante o desenvolvimento deste trabalho.

À minha família, em especial a meus pais Valmir Meneses Albino e Maria Alves da Rocha, que sempre me incentivaram nessa jornada e sempre estiveram ao meu lado.

À minha namorada/noiva, Tássia Brito Andrade, pelo apoio e carinho durante essa jornada.

Aos professores do Departamento de Geotecnia, por todo o conhecimento transmitido, pelas lições profissionais e pela agradável convivência.

Ao grupo GeoInfraUSP por me receber de braços abertos e pela convivência durante essa etapa da minha vida.

Aos colegas de pós-graduação, pela amizade e agradável convivência. Agradeço também os conhecimentos compartilhados durante esses dois anos de convivência.



*"In order to succeed, it is necessary to truly love what you do."*

*"Para se ter sucesso, é necessário amar de verdade o que se faz. "*

(Steve Jobs)



## ABSTRACT

ALBINO, U. R. **The climatic effects on infiltration and stability of geotextile reinforced walls**. 2018. 99 f. Dissertation (Master Degree) – Polytechnic School, University of São Paulo, São Paulo, 2018.

This study presents the climatic effects (rainfall and evaporation) on the stability of reinforced soil walls constructed with nonwoven geotextiles reinforcements using numerical modeling. The evaluation of the climatic effects was organized in two steps: (1) numerical modeling of the infiltration compared to a laboratory full-scale model of a nonwoven reinforced soil wall and; (2) a numerical investigation of a hypothetical geosynthetic-reinforced soil wall subjected to climatic changes including precipitation and evaporation, for a period of 2 years. The numerical modeling of infiltration into the full-scale model was conducted using two representative hydraulic parameters of backfill soil (suction and volumetric moisture content). The infiltration modeling of the laboratory reinforced structure was conducted to provide better understanding around the hydraulic behavior and water path into regions not measured by instrumentation during laboratory tests. Numerical calibration was conducted in order to capture the capillary break developed at soil-geotextile interfaces, including the anchorage of the reinforcements in the wrap-around facing. As a second step of this study, a hypothetical reinforced soil wall constructed with nonwoven geotextile was modeled using the same hydraulic properties of soil and geotextile used in the previously described numerical modeling. The climatic changes were simulated considering the water balance at ground surface. The climatic effects on the reinforced soil wall were assessed by the use of soil suction changes and consequent influences on the factors of safety over 2 years of operation. Results from numerical simulation of infiltration into the laboratory model indicated that water breakthrough did not occur uniformly along the length of the geotextile. In addition, numerical infiltration into the laboratory model showed that the water path into the reinforced zone is influenced by the anchorage of the reinforcement in the wrap-around facing. The results of the climatic variations in the hypothetical structure showed that approximately 50% of potential evaporation and total rainfall effectively evaporates and infiltrates. Also, the results revealed that the capillary barrier did not generate significant surface runoff and did not reduce the effective infiltration in the reinforced zone. On the other hand, water was observed to

advance faster outside of the reinforced zone than inside of the reinforced zone because of the capillary barrier. Additionally, simulations showed that soil inside of the reinforced zone never recovered its initial suction value after first wetting because the capillary barrier restricted evaporation. Results also revealed that increases in global factor of safety, after first wetting of the geotextile reinforced soil wall, occurred because of the increases in soil suction of the first reinforced layer. Lastly, cumulative precipitation during successive days of rainfall showed some correlation to changes in global factor of safety.

Keywords: numerical simulation, infiltration, reinforced soil wall, capillary barrier; climatic changes; geosynthetic

## RESUMO

ALBINO, U. R. **The climatic effects on infiltration and stability of geotextile reinforced walls**. 2018. 99 f. Dissertação (Mestrado) – Escola Politécnica, Universidade de São Paulo, São Paulo, 2018.

Este estudo apresenta os efeitos das variações climáticas (chuva e evaporação) em muros de solo reforçado com geotêxtil não tecido através de análises numéricas. A avaliação dos efeitos climáticos foi dividida em duas fases: (1) calibração numérica da infiltração em um protótipo de laboratório de muro reforçado com geotêxtil não tecido e; (2) extrapolação dos resultados de infiltração para uma estrutura hipotética incluindo as variações climáticas de chuva e evaporação por um período de 2 anos. A calibração numérica foi realizada por meio de duas variáveis (sucção e umidade volumétrica) medidas durante a infiltração no protótipo. Estudos numéricos do processo de infiltração foram conduzidos para melhor entender o comportamento hidráulico da infiltração em regiões que não foram monitoradas durante a infiltração no protótipo. A calibração numérica foi conduzida com o objetivo de capturar o efeito da barreira capilar na interface solo-geotêxtil não tecido, incluindo a ancoragem do reforço próximo a face envelopada. A partir dos resultados da calibração, um muro hipotético reforçado com geotêxtil não tecido foi modelado sob condições climáticas reais (chuva e evaporação), e seu desempenho foi avaliado através das variações de sucção e do fator de segurança ao longo de 2 anos. As variações climáticas foram modeladas considerando o balanço de hídrico na superfície do solo. Os resultados da calibração numérica do modelo de laboratório indicaram que a barreira capilar na interface solo-reforço rompeu de forma não uniforme ao longo do geotêxtil não tecido. Além disso, a avaliação da infiltração mostrou que o fluxo de água tem sua direção afetada pela ancoragem do reforço próximo a face. Os resultados das variações climáticas na estrutura hipotética mostraram que aproximadamente 50% da evaporação potencial e da chuva total efetivamente evapora e infiltra. Além disso, os resultados revelaram que a formação de barreira capilar, e conseqüente retardo na infiltração, não gerou escoamento superficial significativo e não reduziu o volume de água efetivamente infiltrado na zona reforçada. Ademais, as variações de sucção observadas na zona reforçada se mostraram diretamente ligadas aos dias consecutivos de chuva. Por outro lado, observou-se que a frente de umedecimento

avançou mais rápido fora da zona reforçada do que dentro da zona reforçada devido à barreira capilar. As simulações mostraram que o solo dentro da zona reforçada nunca recuperou seu valor inicial de sucção após o primeiro umedecimento porque a barreira capilar restringiu a evaporação. Os resultados também revelaram que o aumento no fator global de segurança, após o primeiro umedecimento do muro reforçado com geotêxtil, ocorreu devido ao aumento da sucção do solo da primeira camada reforçada. Por fim, a precipitação acumulada durante dias consecutivos de chuva mostrou correlação com as mudanças no fator de segurança.

Palavras chave: simulação numérica; infiltração; solo reforçado; barreira capilar; mudanças climáticas; geossintéticos

## LIST OF FIGURES

Figure 2.1 - Layout of full-scale wall with sensor positions .....	30
Figure 2.2 - Backfill, sand and nonwoven geotextile water retention curves .....	33
Figure 2.3 - Backfill soil water retention curve and scanning curve .....	34
Figure 2.4 - Hydraulic conductivity functions: (a) nonwoven geotextile and sand layer; (b) backfill soil and sand layer .....	34
Figure 2.5 - Finite element mesh, boundary conditions and interface element used for the numerical simulation conducted in this study .....	36
Figure 2.6 - Comparison of measured and numerically predicted results of wetting front during capillary barrier effect at instrumented column C1 .....	39
Figure 2.7 - Comparison of experimental and numerical changes in PWP and volumetric water content at different reinforcement layers (RL): (a) RL5; (b) RL4; (c) RL3; (d) RL2; (e) RL1 .....	41
Figure 2.8 - Horizontal sections (1 through 6) and vertical sections (A and B) defined in the reinforced soil wall .....	42
Figure 2.9 - Evaluation of infiltration near secondary reinforcements: (a) PWP contour lines at 5,000 min after infiltration; (b) change in PWP along cross section 6-6 and 5-5 at 5,000, 6,500 and 8,000 min following start of irrigation .....	44
Figure 2.10 - Evaluation of the development of capillary barriers: (a) Ponding of water on top of RL5 (7,400 min); (b) breakthrough at RL5 (13,200 min); (c) ponding of water before water breakthrough at RL4 (15,780 min); (d) breakthrough at RL4 (15,800 min); (e) steady state condition (30,000 min) .....	46
Figure 2.11 - Moistened shotcrete facing at end of experiment.....	46
Figure 2.12 - PWP along RL5 before and after water breakthrough.....	47
Figure 2.13 - Changes in PWP along reinforcement layers when water breakthrough occurred (cross sections 5 to 1, Figure 2.8) .....	48
Figure 2.14 - Vertical profiles of PWP: (a) PWP along cross section A; (b) PWP along cross section B .....	49
Figure 2.15 - Change in PWP along cross sections A and B at interfaces with RL5 to RL1: (a) cross section A, from beginning of numerical simulation; (b) zoom of predicted results from cross section A from 10,000 to 30,000 min; (c) cross section B, from beginning of numerical simulation; (d) zoom of predicted results from cross section B from 10,000 to 30,000 min.....	51

Figure 2.16 - Cumulative drained water volume from numerical analysis: (a) comparison of water drained through shotcrete facing, overflow through top and drainage geocomposites; (b) detailed drainage through shotcrete and overflow through top.....	52
Figure 2.17 - Cumulative water volumes into the reinforced soil wall: soil water storage, applied irrigation and water outflow. ....	53
Figure 3.1 - Period of analyses for evaluation of climate change effects .....	63
Figure 3.2 - Daily rainfall, relative humidity and temperature between 2013 and 2014 .....	64
Figure 3.3 - Geosynthetic reinforced soil wall section.....	65
Figure 3.4 - Backfill and nonwoven geotextile water retention curves adopted from Albino <i>et al.</i> (2018).....	68
Figure 3.5 - Unsaturated hydraulic conductivity of soil and nonwoven geotextile .....	68
Figure 3.6 - Illustration of GRS model and observational sections .....	69
Figure 3.7 - Details of boundaries and properties for infiltration and evaporation simulations.....	70
Figure 3.8 - Illustration of the entry and exit search method with the respective areas location used in this study.....	72
Figure 3.9 - Water balance over two years of climate analysis .....	75
Figure 3.10 - Precipitation change in pore water pressure and global factor of safety .....	78
Figure 3.11 - Nonwoven geotextile (NWG) influence in water advancement.....	80
Figure 3.12 - (a) Suction profiles 7 m from wall face (section C); (b) Suction profiles 3 m from wall face (section B); (c) Changes in net infiltration over 89 days of climatic analyses.....	82
Figure 3.13 - (a) Pore water pressure distribution after 39 days of climatic analyses; (b) The factor of safety after 39 days of climatic analyses .....	83
Figure 3.14 - (a) Water ponding starting on day 34; (b) Prior to breakthrough of water .....	84
Figure 3.15 - Suction profile for different days. (a) 7 m from wall face (section C, see Figure 3.6); (b) 3 m from wall face (section B, see Figure 3.6) .....	86
Figure 3.16 - Relationship of cumulative precipitation during consecutive rainy days with the factor of safety .....	87

## LIST OF TABLES

Table 2.1 - Characteristics of compacted backfill, geosynthetic and guidelines for backfill of reinforced wall .....	31
Table 2.2 - Model and equations used to adjust water retention curves and predict hydraulic conductivity functions .....	32
Table 2.3 - Soil and geosynthetic hydraulic parameters .....	32
Table 3.1 - Characteristic properties of soil and geotextile .....	66



## SUMMARY

1. INTRODUCTION.....	23
1.1 Objectives .....	24
1.2 Structure.....	24
2. NUMERICAL SIMULATION OF INFILTRATION INTO THE FILL OF A WALL REINFORCED WITH NONWOVEN GEOTEXTILES .....	25
2.1 Introduction and background.....	26
2.2 The laboratory full-scale wall.....	29
2.3 Hydraulic properties of materials.....	31
2.4 Numerical simulation of the infiltration process .....	34
2.5 Results and discussions.....	36
2.5.1 Scanning curves .....	36
2.5.2 Comparison between experimental results and numerical predictions ..	38
2.6 Use of numerical simulation to extend interpretation of infiltration process into non-instrumented zones of the reinforced soil wall .....	41
2.7 Water infiltration near the secondary reinforcements resulting from wrap- around facing .....	42
2.8 Development of capillary barriers and generation of positive pore water pressures.....	44
2.9 Location of water breakthrough.....	46
2.10 Analysis of pore water pressure profiles.....	48
2.11 Pore water pressure development at geotextile interface.....	49
2.12 Cumulative water volume through different elements of the face.....	51
2.13 Conclusions.....	53
3. NUMERICAL SIMULATION OF INFILTRATION GEOTEXTILE-REINFORCED SOIL WALL CONSIDERING SOIL-ATMOSPHERE INTERACTION.....	57
3.1 Introduction .....	57
3.2 Methodology to apply rainfall and evaporation .....	61
3.2.1 Modelling of soil-atmosphere interaction .....	61
3.2.2 Simulation of actual evaporation.....	62
3.3 Climatic changes consideration.....	63
3.4 Numerical model of a GRS wall .....	64
3.4.1 GRS wall section .....	64
3.4.2 Soil and Geosynthetic modelling (characteristics) .....	65

3.4.3	Infiltration modelling .....	68
3.5	Global stability analysis .....	71
3.6	Results and Discussion .....	73
3.6.1	Soil-atmosphere interaction.....	73
3.6.2	Climate effects on pore water pressure and global factor of safety.....	76
3.7	Conclusions .....	87
4.	GENERAL REMARKS.....	91
	REFERENCES .....	93

## 1. INTRODUCTION

Geosynthetics are currently an economical attractive solution which has been used worldwide as reinforcement, to control soil erosion, to separate materials of different grain size distribution and other applications. The advance in technology and the challenges in the current engineering practice has required the academy to improve the applicability of such a versatile material, as the geosynthetic. Therefore, its applicability in adverse situations has been studied by many researchers during the last decades.

The application of geosynthetic has the advantage of being a flexible material, which make field placement easier when compared to rigid steel strips. Besides that, some geosynthetics can be used for more than one application. Nonwoven geotextile is an example of a geosynthetic that can be used for separation, filtration, reinforcement and drainage. This wide range of applications are due to the porous matrix, which nonwoven geotextile is formed. Moreover, according to Mitchell e Zornberg (1995) nonwoven geotextiles can be used to replace conventional drainage systems of granular material providing about 40% cost savings due to back fill availability near to site construction.

As explained previously, nonwoven geotextiles can comply with more than one need (e.g. reinforcement, drainage, separation, etc.), so that it makes this material attractive when constructing soil reinforced wall with poorly drainage backfill. Although, researchers (Erlich, Vidal and Carvalho, 1997) showed the outstanding confined stiffness of the nonwoven geotextile by comparing the performance of two slopes reinforced with woven and nonwoven geotextiles, in the current geotechnical engineering practice, the use of nonwoven geotextile is still discredited because of its low unconfined tensile stiffness. Therefore, nonwoven geotextiles are replaced by geogrids in order to avoid large deformations.

Despite the fact that nonwoven geotextile is an extensible material, recent research studies have shown that, its use in a reinforcement and drainage role provided good performance during the soil structure life time (MITCHELL; ZORNBERG, 1995; PORTELINHA et al., 2013, 2014; PORTELINHA; ZORNBERG, 2017). Additionally, the nonwoven geotextile was found to improve overall structural stability (IRYO; ROWE, 2005a; THUO et al., 2015, 2016). On the other hand, these previously mentioned studies showed that nonwoven geotextile retard water flow due

to capillary effect at soil-geotextile interface. The capillary effect was found to increase water content above the nonwoven geotextile and cause the increasing of positive pore water pressure. This behavior is not desired and cause the soil-reinforcement shear strength to reduce leading to local failure or large deformation.

The present study was conducted to show important aspects regarding the use of nonwoven geotextile to reinforced soil reinforced structures when subjected to climatic changes. The study includes the numerical calibration of a reinforced soil wall prototype subjected to constant rainfall and extrapolation of the results to a hypothetical field reinforced wall under real climate conditions. Aspects such capillary effect, pore water pressure changes and changes in factor of safety are discussed.

## **1.1 Objectives**

Based on the aspects shown before, this study aimed to show the behavior of nonwoven geotextile reinforced soil structures when subjected to climate conditions throughout numerical simulations. The specific objectives of the present study were:

1. Evaluate, through numerical simulations, the infiltration process into a reinforced soil wall prototype in regions that were not monitored during the laboratory experiment conducted by Portelinha and Zornberg (2017);
2. Comprehend the overall stability of a nonwoven geotextile reinforced soil wall when subjected to 2 years of climatic changes;

## **1.2 Structure**

This study was divided into four chapters. Chapter two and three were constructed to answer each specific objective and with the structure of a journal article for publication purpose. Chapter four includes the main conclusion of chapter two and three.

## **2. NUMERICAL SIMULATION OF INFILTRATION INTO THE FILL OF A WALL REINFORCED WITH NONWOVEN GEOTEXTILES**

### **Abstract**

While the backfill of geosynthetic-reinforced soil structures is generally specified to be free-draining, the use of fine-grained backfill materials has started being considered when nonwoven geotextiles with in-plane drainage capabilities are used as reinforcement elements. However, water infiltration into the fine-grained backfill of geotextile-reinforced structures may still be of concern due to the development of unsaturated hydraulic mechanisms, such as capillary barriers, which have been reported to occur at the interface between soil and geotextiles. In this chapter, a numerical investigation on water infiltration into the fine-grained backfill of a large-scale wall reinforced using nonwoven geotextiles. The large-scale wall was constructed in laboratory and fully instrumented to measure changes in volumetric water content and soil suction while the structure was subjected to irrigation. The numerical investigation was performed to gain insight into the overall infiltration process, with particular focus on the hydraulic behavior at soil-geosynthetic interfaces that were not properly captured in the laboratory model, including capillary effects, location of breakthrough along the reinforcement length and the effect of the wrap-around facing. The numerical results revealed that the three-dimensional problem (laboratory test) may not be accurately simulated with a two-dimensional analysis (numerical modelling), particularly to quantify the capillary ponding effects. Overall, numerical analyses were found to agree to the experimental results. The results also indicated that the use of nonwoven geotextile may retard water flow into subsequent layers and breakthrough of water not occurring uniformly along the length of the geotextile. The study allows to observe the significant contribution of the length of reinforcement anchorage in the wraparound facing changing the water flow direction towards the wall facing. Also, the capillary effects in geotextile reinforced soil structures were found to be significant affected by the heterogeneity of soil porosity due to compaction.

## 2.1 Introduction and background

The use of nonwoven geotextiles to reinforce poorly draining soils have been extensively investigated over the last decades through laboratory tests, field investigations and numerical analyses (TATSUOKA; YAMAUCHI, 1986; ZORNBERG; MITCHELL, 1994; MITCHELL; ZORNBERG, 1995; IRYO; ROWE, 2005a; PORTELINHA et al., 2013; THUO et al., 2015; YANG et al., 2018). The use of geosynthetics with in-plane drainage capabilities, such as nonwoven geotextiles, has been considered as a possible approach to allow the use of fine-grained soils as backfill material in reinforced soil structures. However, the infiltration into geotextile-reinforced structures has remained as a concern due considerations such as the progressive loss of soil suction, the development of pore water pressures (PWP) and specific hydraulic effects (e.g. the development of a capillary barrier) at the soil-geosynthetic interface. A number of studies have reported the use of nonwoven geotextiles to dissipate PWP and acting as a drain when properly installed and when the surrounding soil is nearly saturated (TAN et al., 2001; IRYO; ROWE, 2003, 2005a; THUO; YANG, 2014; BHATTACHERJEE; VISWANADHAM, 2015; THUO et al., 2015). Some researchers have reported that nonwoven geotextile may act as a water barrier which is resulting of capillary effects due to water retention characteristics of both the soil and nonwoven geotextile (STORMONT; MORRIS, 2000; IRYO; ROWE, 2004; MCCARTNEY; ZORNBERG, 2010; ZORNBERG et al., 2010; THUO et al., 2015, 2016; PORTELINHA; ZORNBERG, 2017; LIMA et al., 2018). Also, loss of soil suction in reinforced soil structures when subjected to infiltration has also been identified as a concern due to its effect on wall performance (IRYO; ROWE, 2005a; PORTELINHA et al., 2013; ESMAILI et al., 2014; HATAMI; ESMAILI, 2015; BALAKRISHNAN; VISWANADHAM, 2016; VAHEDIFARD et al., 2016; PORTELINHA; ZORNBERG, 2017; YANG et al., 2018). However, experimental studies (BUENO et al., 2005; BENJAMIM et al., 2007; PORTELINHA et al., 2013, 2014; PORTELINHA; ZORNBERG, 2017) published to date have reported that although the wetting advancement into the reinforced soil structure tended to increase reinforcement strain and reduce matric suction, the overall performance of the reinforced soil using nonwoven geotextiles has been satisfactory.

Loss in matric suction is directly related to infiltration into the reinforced soil structure. In retaining structures reinforced using nonwoven geotextiles, a reduction in

matric suction is intensified by the development of a capillary barrier at the soil-geotextile interface. A capillary barrier develops when two unsaturated materials with different pore structures are in contact. More precisely, a material of comparatively small pores overlying a material of comparatively large pores with different unsaturated hydraulic conductivities leads to the development of this phenomenon. The material with comparatively large pores can be either a coarse-grained soil or a nonwoven geotextile. Capillary barriers have been reported to be beneficial in a number of different applications, such as landfill covers (ANDERSON, 1997; MELCHIOR, 1997; MORRIS; STORMONT, 1997; LI et al., 2013; ZHAN et al., 2014; NG et al., 2015; RAHARDJO et al., 2016; LIMA et al., 2018), water storage in agriculture (ITYEL et al., 2011, 2012; EL-NESR et al., 2014) and water migration in pavements (HENRY; HOLTZ, 2001; STORMONT et al., 2001). Conversely, capillary barriers have also been reported as having a negative impact on the performance of structures such as retaining wall reinforced using nonwoven geotextiles due to water accumulation over the interface (IRYO; ROWE, 2004, 2005a, 2005b; ZORNBERG et al., 2010; THUO et al., 2015; PORTELINHA; ZORNBERG, 2017; YANG et al., 2018).

A number of studies (STORMONT; MORRIS, 2000; IRYO; ROWE, 2003, 2004, 2005a, 2005b; GARCIA et al., 2007; MCCARTNEY; ZORNBERG, 2010; ZORNBERG et al., 2010; BAHADOR et al., 2014; PORTELINHA; ZORNBERG, 2017) have shown that the nonwoven geotextile drainage function is considerably diminished under unsaturated conditions and the capillary barrier effect may occur, facilitating a loss in matric suction. As a result, low stiffness reinforced soils (e.g. structures reinforced using nonwoven geotextiles) are expected to experience large displacements.

Two-dimensional transient infiltration in reinforced soil structure has been investigated using numerical techniques in several studies (IRYO; ROWE, 2005a; THUO et al., 2015; CHINKULKIJNIWAT et al., 2017; YANG et al., 2018) in the last decade. Generally, these studies have evaluated the performance or stability of nonwoven geotextile-reinforced soil structures during artificial rainfalls. For instance, Iryo and Rowe (2005a) studied the effect of an artificial rainfall on the performance of an unreinforced and three reinforced sand embankments constructed using different nonwoven geotextile configurations. Numerical results showed good agreement with experimental results and confirmed a high degree of saturation near the nonwoven geotextile-backfill soil interface. Furthermore, the nonwoven geotextile drainage

function was reported to be ineffective, with nearly positive PWP being developed. Thuo et al. (2015) conducted numerical analyses with different infiltration rates using information from a reinforced slope reported by the Public Works Institute (PWRI), Japan (also studied by Iryo and Rowe (2005a)), with and without sand cushions surrounding the nonwoven geotextile (i.e. a geotextile within thin layers of highly permeable sand). Results showed that the presence of an intermediate material (i.e. sand cushion) reduced the capillary barrier effect significantly and consequently prevented buildup of moisture above the nonwoven geotextile. Moreover, local and overall stability were improved due to the presence of sand cushions. Yang et al. (2018) performed a series of numerical analyses to investigate the hydraulic response and stability of reinforced soil slopes with various backfill types (e.g. sand, silt and silty clay), reinforcement types (e.g. geogrid, geotextile) and rainfall intensities (e.g. 350 and 500 mm per day). Additionally, the efficiency of sand cushions, in terms of factor of safety, was also evaluated for the case of clay slopes to determine an optimum design in terms of sand cushion thickness. Results showed that the performance of poorly draining backfills is highly affected by the ratio of rainfall intensity and saturated hydraulic conductivity of the backfill (i.e.  $q/k_s$ ). Local stability was found to be more affected when cohesive soils were used as backfill due to the development of capillary barriers. As a solution to the increase in moisture due to the capillary barrier effect, an optimal sand cushion thickness of 15 cm was identified, which corresponds to the maximum thickness at which the drainage function has contributed maximally to local as well as global stability.

In summary, numerical investigations involving infiltration into geosynthetic-reinforced soil structures documented in literature (IRYO; ROWE, 2005a; THUO et al., 2015; YANG et al., 2018) have involved no, or limited experimental data for comparison with numerical simulations. In addition, scarce are the researches that provide the fully investigation of capillary effects on unsaturated interfaces between drained reinforcements and fine-grained backfill soils. Consequently, this study includes comparison of extensive instrumentation data reported by Portelinha and Zornberg (2017) with the results of numerical predictions involving a two-dimensional infiltration into a geotextile-reinforced soil structure. Instrumentation data was collected by sensors monitoring the advancement of wetting and changes in matric suction along the height of a reinforced wall, yielding reliable results. This study also investigates the

infiltration into reinforced zones not monitored in the laboratory reinforced soil wall, providing additional information to properly understand the wall performance.

## 2.2 The laboratory full-scale wall

The laboratory full-scale wall constructed as part of this study involved a reinforced wall with a height of 1.8 m, a width of 1.55 m and a depth of 1.8 m (see Figure 2.1). The backfill soil was contained within a steel frame bolted to a structural concrete base. Nonwoven geotextiles with a length of 1.55 m were installed using a vertical spacing of 300 mm and a 1% incline toward the facing to facilitate in-plane drainage. The wall facing involved shotcrete placed over the wraparound facing. Two horizontal layers of drainage geocomposites were installed at the face to facilitate drainage. The reinforced wall was subjected to uniform infiltration, which was imparted using a series of pipes. The resulting inflow was uniformly distributed, as achieved by using a drainage sand layer overlain by a geocomposite. Water was applied from the top of the wall at a rate  $q = 1.8 \times 10^{-7}$  m/s, which corresponded to a fraction of the backfill saturated hydraulic conductivity (specifically,  $0.37 k_{sat \text{ backfill}}$ ). Water content sensors (FDR) were used to measure the advancement of water through the geotextile-reinforced wall. Water content sensors were concentrated in the top reinforcement layer (RL5) in particular to capture the development of the capillary barrier. In addition, one water content sensor and one tensiometer were located at the mid-height of each subjacent reinforcement layer to measure the advancement of water and soil suction changes during irrigation. Tensiometers were placed 50 mm above each reinforcement layer. Figure 2.1 illustrates the instrument locations in the full-scale model. Additional details on the large-scale model and instrumentation are reported in Portelinha and Zornberg (2017).

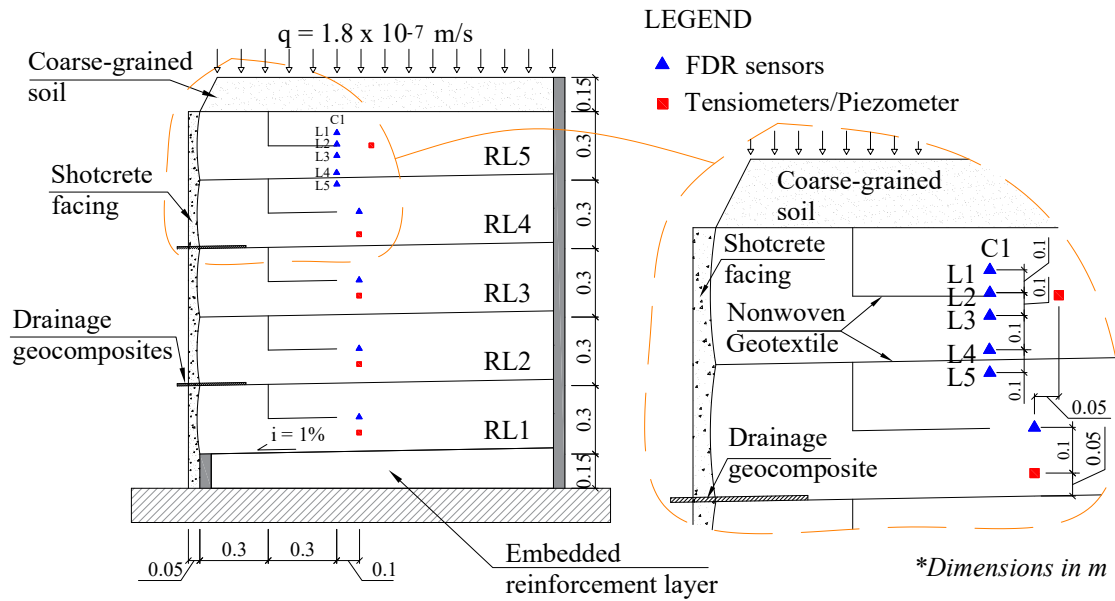


Figure 2.1 - Layout of full-scale wall with sensor positions  
Source: modified from Portelinha and Zornberg (2017)

The backfill material used in the large-scale model was a brown lateritic soil from a deposit in São Carlos, São Paulo, in southeastern Brazil. Lateritic soils are considered good material for the construction of roads, highways, airfields, earth dams, foundations of structures (GIDIGASU, 1976) and for use as backfill of retaining structures. Different from sedimentary clays, fine-grained lateritic soils are also known to have low permeability and optimum water content after compaction, as well as, high maximum unit weight. According to the Unified Soil Classification System (USCS) (ASTM D2487, 2011), the soil classifies as a clayey sand (SC). Table 2.1 shows the characteristics of the compacted backfill used in the large-scale model, the geosynthetic characteristics and typical guidelines for selection of marginal backfill materials of reinforced wall. As indicated in this table, both Federal Highway Administration (FHWA, 2009) and National Concrete Masonry Association (NCMA, 2016) recommend marginal backfill with up to 35% passing a No. 200 (0.075mm) sieve. Additionally, National Concrete Masonry Association (NCMA, 2016) recommend the backfill with a plasticity index (PI) less than 20 and liquid limit (LL) less than 40 providing the reinforced wall height less than 3 m. Table 2.1 also shows that the backfill soil used in the experiment does not fully comply with both guidelines recommendation regarding the selection of marginal backfill for reinforced soil wall.

Table 2.1 - Characteristics of compacted backfill, geosynthetic and guidelines for backfill of reinforced wall

Material	Characteristics	Values	Guidelines for marginal backfill	
			FHWA (2009)	NCMA (2016)
Backfill soil	Clay fraction	32%	-	Silt + Clay < 35%
	Silt fraction	12%		
	Sand fraction	56%	-	Sand > 20%
	G <sub>s</sub>	2.75	-	-
	LL	40%	-	LL < 40%
	PL	19%	-	-
	PI	21%	-	PI < 20%
	D <sub>85</sub>	0.32 mm	-	-
	D <sub>50</sub>	0.11 mm	-	-
	γ <sub>d</sub> <sup>max</sup>	17.9 kN/m <sup>3</sup>	-	-
	W <sub>opt</sub>	14.6%	-	-
	k <sub>sat</sub>	4.9 × 10 <sup>-7</sup> m/s	-	-
Nonwoven geotextile	Weight per unit area	293 g/m <sup>2</sup>		
	Thickness	3.00 mm		
	Permittivity	1.96 s <sup>-1</sup>		
	Porosity	0.94		

Source: modified from Portelinha and Zornberg (2017)

### 2.3 Hydraulic properties of materials

Water retention curves for the nonwoven geotextile were obtained using the procedure proposed by Krisdani et al. (2008). The procedure consisted of hanging strips of geotextile 5 mm wide and 100 mm long in a vertical position with a length of 20 mm submersed in a water container. The capillary rising was monitored and obtained by the determination of water content along the geotextile strip. The wetting path of the geotextile water retention curves was obtained using air-dried strips and the drying path was obtained by saturating the strip prior to testing. For the drying path, the nonwoven geotextile was saturated by soaking the strip in water inside a vacuum pycnometer for more than 24 h. Geotextile strips remained hanging for 24 hours to reach equilibrium, as recommended by Krisdani et al. (2008), and were then cut into 5 mm long pieces and oven-dried to measure the water content. The matric suction was calculated based on the elevation of the specimen above the water table.

The soil water retention curve was obtained using the filter paper technique (ASTM D5298, 2012) and hanging column tests (ASTM D6836, 2012), considering both drying and wetting processes. Because the lateritic backfill soil showed a heterogeneous pore distribution, Durner's (1994) model was found to properly fit the experimental data. Durner's model (1994) involves the superposition of two unimodal retention curves defined using the van Genuchten (1980) model. The hydraulic conductivity functions of both the soil and nonwoven geotextile were predicted using Mualem's (1976) model. Table 2.2 presents the models and equations used for water retention characterization.

Table 2.2 - Model and equations used to adjust water retention curves and predicted hydraulic conductivity functions

Model	Equation
Durner (1994)	$\Theta = w_1 \left[ \frac{1}{1 + (\alpha_1 \psi)^{n_1}} \right]^{m_1} + (1 - w_1) \left[ \frac{1}{1 + (\alpha_2 \psi)^{n_2}} \right]^{m_2} \quad (2.1)$
van Genuchten – Mualem's (1980)	$\Theta = \frac{\theta - \theta_r}{\theta_s - \theta_r} = \left( \frac{1}{1 + (\alpha \psi)^n} \right)^m \quad (1.2)$
	$k = k_{sat} \Theta^{1/2} \left[ 1 - \left( 1 - \Theta^{1/m} \right)^m \right]^2 \quad (2.3)$

where  $\Theta$  is the normalized volumetric water content;  $w_1$  and  $w_2$  are the initial gravimetric water content of each segment of the soil bimodal water retention curve;  $\psi$  is the matric suction;  $\theta_s$  is the saturated volumetric water content;  $\theta_r$  is the residual volumetric water content;  $n$ ,  $m$  and  $\alpha$  are the curve fitting parameters; and  $k$  is the hydraulic permeability.

Fitting parameters of the soil and geotextile are summarized in Table 2.3.

Table 2.3 - Soil and geosynthetic hydraulic parameters

Material Parameter	Backfill soil <sup>a</sup>		Nonwoven geotextile	
	Drying path	Wetting path		
$\theta_s$ (m <sup>3</sup> /m <sup>3</sup> )	0.35741	0.34497	0.65000	0.45050
$\theta_r$ (m <sup>3</sup> /m <sup>3</sup> )	0.00000	0.00000	0.00000	0.00000
$w_1$	0.29413	0.4988	-	-
$\alpha_1$ (kPa <sup>-1</sup> )	0.11238	0.0001	1.90949	3.29674
$n_1$	4.6831	3.87213	2.90125	7.63205
$m_1$	0.78646	0.74174	0.65532	0.86897
$\alpha_2$ (kPa <sup>-1</sup> )	0.00014	0.7681	-	-
$n_2$	2.425	1.3041	-	-
$m_2$	0.58763	0.23319	-	-
$k_{sat}$ (m/s)	4.90×10 <sup>-7</sup>		5.80×10 <sup>-3</sup>	

<sup>a</sup>Obtained from experimental data presented in Portelinha and Zornberg (2017)

The experimental results in Figure 2.2 show the water retention curves for both materials, emphasizing the difference between the water retention for the nonwoven geotextile and backfill soil. For example, for a matric suction of 10 kPa the nonwoven geotextile is practically dry, while the backfill soil is essentially saturated. Figure 2.2 also shows the water retention curve of the drainage cushion (sand) used to distribute the irrigation water over the top of the reinforced soil wall. The drainage cushion (sand) water retention curve was assumed to be well represented by the predefined sand function available in the SEEP/W database (GEO-SLOPE, 2018a). Water retention curve of the sand was estimated assuming soil porosity of 0.45 and hydraulic conductivity of  $1.0 \times 10^{-4}$  m/s. Similar values of  $k_{sat}$  of sands are published in literature (RAISINGHANI; VISWANADHAM, 2010; LI et al., 2013; YANG et al., 2018). Figure 2.3 shows the complete drying and wetting path of the backfill soil used as backfill in the experiment.

A comparison between the hydraulic conductivity function of the nonwoven geotextile and that of the sand is presented in Figure 2.4a. In addition, Figure 2.4b shows a comparison between the sand hydraulic conductivity function and that of the backfill soil. Figure 2.2, 2.3 and 2.4 will be discussed further following an explanation of the scanning curves.

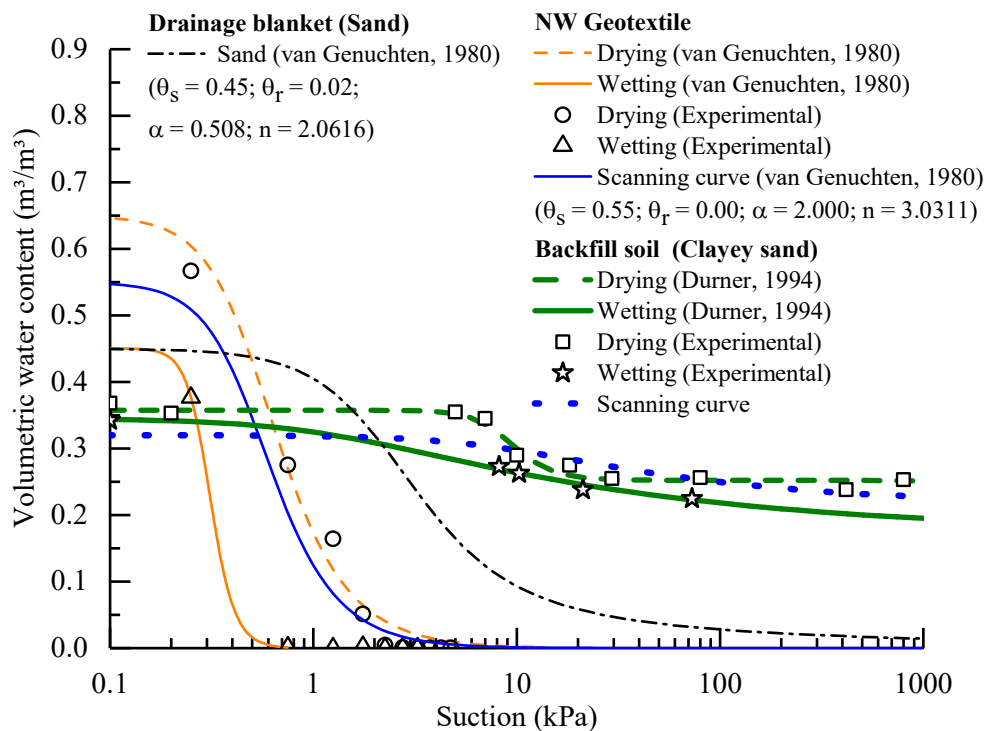


Figure 2.2 - Backfill, sand and nonwoven geotextile water retention curves

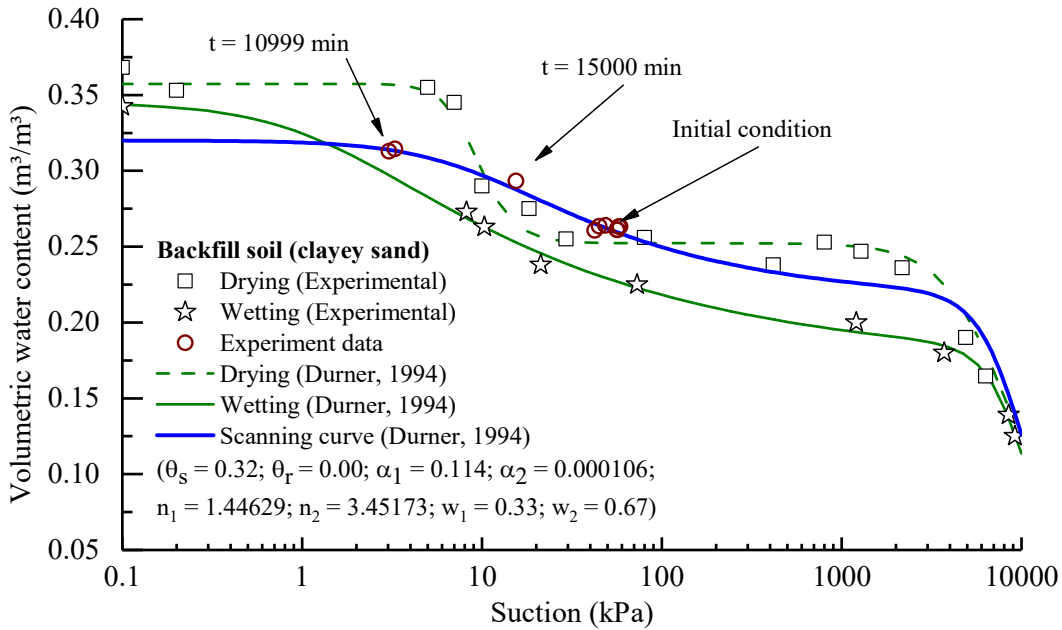


Figure 2.3 - Backfill soil water retention curve and scanning curve

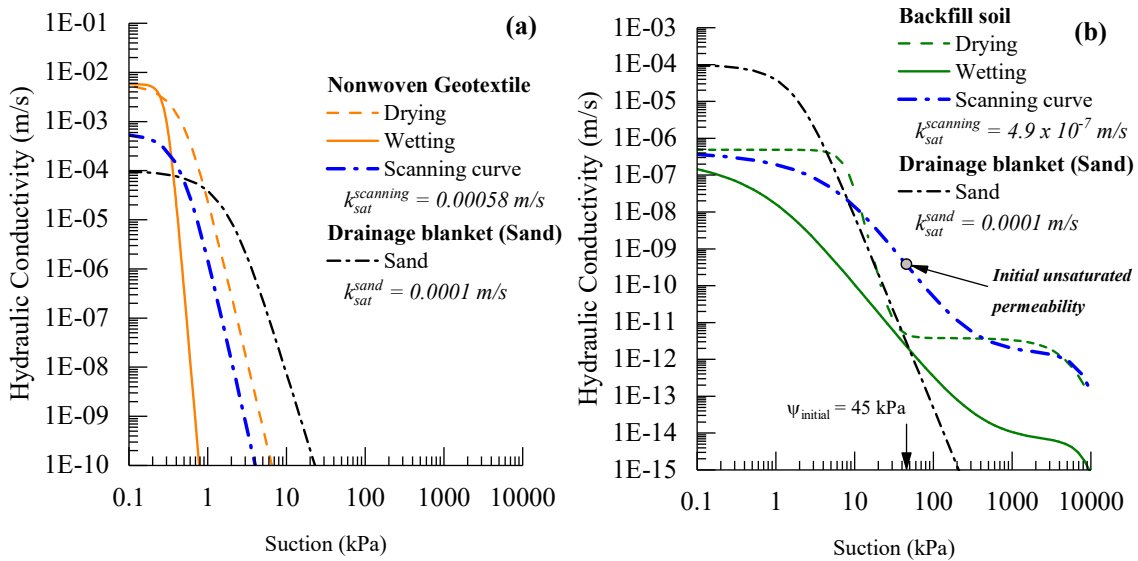


Figure 2.4 - Hydraulic conductivity functions: (a) nonwoven geotextile and sand layer; (b) backfill soil and sand layer

## 2.4 Numerical simulation of the infiltration process

An infiltration process was modeled as part of this study to facilitate a thorough evaluation of the unsaturated flow into the large-scale geotextile-reinforced soil structure detailed previously (Figure 2.1). Focus was placed on the development of the capillary barrier, internal drainage provided by the nonwoven geotextiles and progress of water infiltration into the wall. Due to the comparatively higher density of volumetric water content sensors in the upper reinforcement layer (RL5), monitoring data from

this layer was used to calibrate the numerical modeling. The finite-element software SEEP/W (GEO-SLOPE, 2018a) was used to solve a form of Richards' (1931) two-dimensional equation for transient infiltration modeling, as described by:

$$m_w \frac{\partial(u_a - u_w)}{\partial t} = \frac{\partial}{\partial y} \left[ \left( \frac{k_y}{\gamma_w} \right) \frac{\partial u_w}{\partial y} + k_y \frac{\partial y_e}{\partial y} \right] + \frac{\partial}{\partial x} \left[ \left( \frac{k_x}{\gamma_w} \right) \frac{\partial u_w}{\partial x} + k_x \frac{\partial y_e}{\partial x} \right] \quad (2.4)$$

where  $k_x$  and  $k_y$  are the hydraulic conductivity in x and y directions, respectively;  $u_w$  is the pore water pressure;  $u_a$  is the pore air pressure;  $y_e$  is the elevation;  $\gamma_w$  is the unit weight of water; and  $m_w$  is the coefficient of water volume change (slope of the soil water retention curve).

The reinforced soil wall was modeled using triangular elements with global height of 25 mm. A total of 11,105 triangular elements and 6,141 nodes were automatically created by the mesh generator available in SEEP/W (GEO-SLOPE, 2018a). The nonwoven geotextile was modeled using 3 mm-thick line elements with prescribed hydraulic properties. Similarly, the shotcrete facing and nonwoven geotextile at the wall face were modeled as 12 mm-thick line elements. Figure 2.5 shows the numerical model mesh, boundary conditions and details of the nonwoven geotextile. Water irrigation on top of the wall was reduced from  $1.8 \times 10^{-7}$  m/s to  $1.0 \times 10^{-7}$  m/s because the overflow occurring through the sand layer was much higher than observed during the experiment. Also, the higher water outflow indicates that the applied vertical stress and soil particles surrounding the pipes could reduce the actual water irrigation during the experiment. Comparison of experimental and numerical soil water storage are presented in the discussion section to ensure that the adopted reduction is reasonable. The wall face (Figure 2.5) was adopted as a permeable boundary condition (i.e. potential seepage face) from where water drained out of the domain if the PWP reached positive values at those nodes.

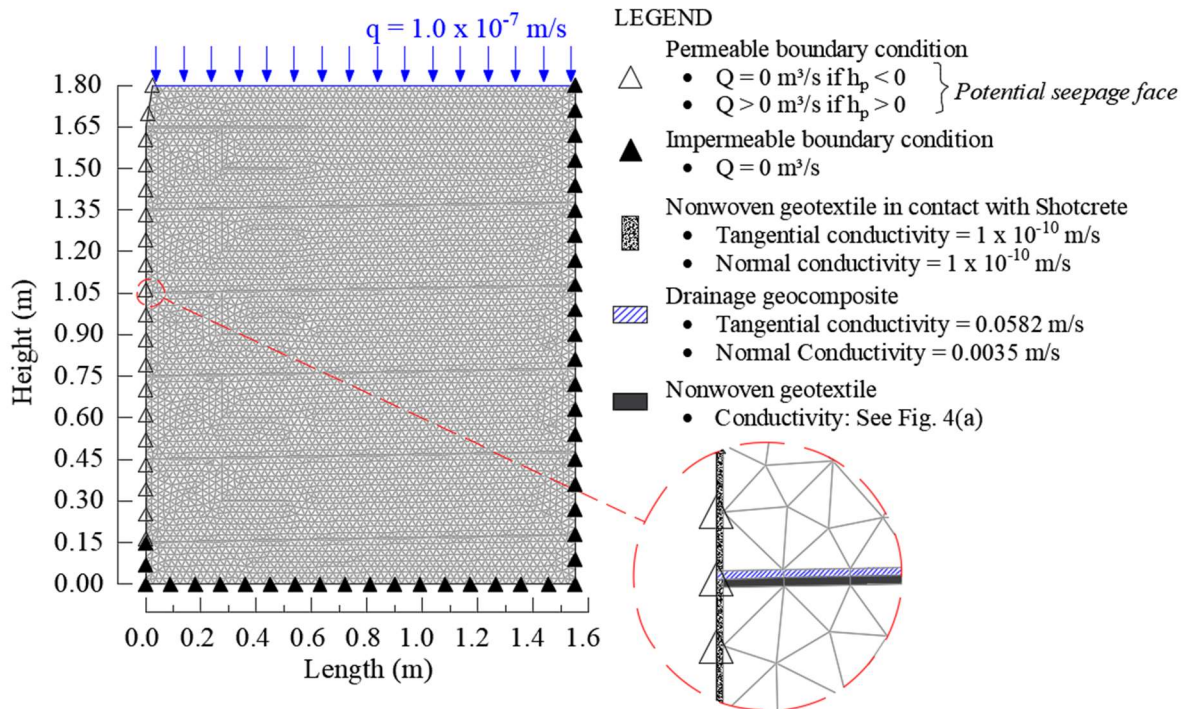


Figure 2.5 - Finite element mesh, boundary conditions and interface element used for the numerical simulation conducted in this study

Furthermore, because 15 cm of RL1 were embedded in the floor, an impermeable boundary condition was adopted at this elevation in the numerical model. The back of the wall was also adopted as impermeable boundary conditions. Since the wall face involved a wrap-around nonwoven geotextile protected by a shotcrete facing, a hydraulic conductivity of  $1.0 \times 10^{-10} \text{ m/s}$  was assumed in the numerical modeling, which is consistent with the magnitude of concrete hydraulic conductivity reported in Roy (1989), Holmén and Stigsson (2001), and Luna *et al* (2006).

## 2.5 Results and discussions

### 2.5.1 Scanning curves

Figure 2.2, 2.3 and 2.4 also show the curves obtained from the adequate agreement between experimental and numerical results (scanning curves) which were observed to be limited by the main drying and wetting curves. These curves have been labeled in many studies (KOOL; PARKER, 1987; IRYO; ROWE, 2004; MAVROULIDOU; GUNN, 2007; TAMI; RAHARDJO, 2007; MCCARTNEY; ZORNBERG, 2010; YVONNE LINS, YAZHOU ZOU, 2013; CUOMO *et al.*, 2017) as the scanning curves, which represent the hysteresis occurring during wetting and

drying cycles. The soil scanning curve was obtained using volumetric water content and tensiometer readings during tests in the full-scale model, which were considered as suitable conditions representing the hydraulic parameters during infiltration processes. Based on the reported sensor readings, the initial condition of the backfill soil was determined to be  $\theta_i = 26\%$  and  $\psi_i = 45$  kPa. A steady state condition was considered to be achieved 25,000 minutes following the beginning of infiltration, when the backfill soil reached conditions corresponding to  $\theta = 31\%$  and  $\psi = 3.04$  kPa. In addition, an intermediate time at 15,000 minutes following the start of infiltration was used as a time for calibration purpose. This selection was adopted to confirm that numerical simulation of the infiltration process was consistent with monitored data from its initial to its final (steady state) conditions. For suction values higher than 46 kPa, the water retention curve was adjusted to have a shape similar to that of the wetting curve. The nonwoven geotextile scanning curve was adjusted by adopting  $\theta_s = 55\%$  and  $\theta_r = 0\%$ , and varying the fitting parameters  $n$  and  $\alpha$  of the van Genuchten-Mualem model (1980). The saturated volumetric water content was adopted as 55% to account for the air and soil particles entrapped in the geotextile. The range of possible variation of each fitting parameter (i.e.  $n$  and  $\alpha$ ) adopted in this evaluation was:  $2.90125 \leq n \leq 7.63205$  and  $1.90949 \text{ kPa}^{-1} \leq \alpha \leq 3.29674 \text{ kPa}^{-1}$ , with these ranges being defined based on the drying and wetting curves (Table 2.3).

The scanning curves for both the soil and nonwoven geotextile, and their respective parameters, are presented in Figure 2.2 and Figure 2.3. Figure 2.4a shows that the hydraulic conductivity of the geotextile scanning curve, which is conventionally deduced from a permittivity test, was decreased by one order of magnitude to achieve good agreement between numerical and experimental results in terms of capillary barrier. A similar decrease was also adopted by Siemens and Bathurst (2010) and Iryo and Rowe (2004) to account for the influence of particle intrusion and match the physical results. Particle intrusion has been reported to reduce the hydraulic conductivity of nonwoven geotextiles (PALMEIRA; GARDONI, 2000; MISZKOWSKA et al., 2017). Figure 2.4b shows that no changes were considered in relation to the saturated hydraulic conductivity of the backfill soil. Trapped air is a problem that should be accounted for in the saturated hydraulic conductivity of the backfill. However, in this study, the trapped air was not assumed to cause a change in the compacted backfill

saturated hydraulic conductivity, but only to change the saturated volumetric water content, as shown in Figure 2.2 and Figure 2.3.

Figure 2.2 also shows that the nonwoven geotextile, represented by its scanning curve, started to saturate when suction decreased to less than 1.5 kPa. Around this magnitude of suction, Figure 2.4a indicates that the predicted hydraulic conductivity of the nonwoven geotextile was around  $10^{-8}$  m/s, or rather that the nonwoven geotextile was practically impermeable by the time it started to moisten. Additionally, Figure 2.3 and Figure 2.4b show that when matric suction was around 1.5 kPa, the backfill soil was practically saturated, with a hydraulic conductivity of  $10^{-7}$  m/s. From these observations, it can be concluded that water will move 10 times slower into the geotextile than into the backfill soil. This explains why water starts to accumulate on top of the nonwoven geotextile before break of the capillary barrier occurs, causing the backfill overlying the geotextile to reach moisture content values close to saturation.

### 2.5.2 Comparison between experimental results and numerical predictions

Figure 2.6 shows a comparison between the experimental results from the instrumented layer C1 (Figure 2.1) and the corresponding numerical prediction. The results show that the numerical model was able to predict the advancement of the water front and capture the development of the capillary barrier, as indicated by the adequate agreement between experimental and numerical data, particularly regarding overall trend and magnitude of moisture content values. The discrepancies between measured and predicted moisture content values may also be attributed to soil heterogeneity resulting from the compaction process, which may have affected the soil void ratio in the vicinity of the reinforcement layer. A more significant discrepancy can be observed regarding the time history of the volumetric water content information, which can be observed by the time of arrival of the moisture front (wetting velocity) at a given location. This is more evident for the case of the sensor located below the nonwoven geotextile (L5). Such discrepancy can be attributed to the theoretical nature of the hydraulic conductivity functions, which were defined based strictly on conceptual models rather than experimental results. Nonetheless, the discrepancy in time-history is not believed to affect the main aspect of the numerical simulation, which centers on the development of capillary barriers.

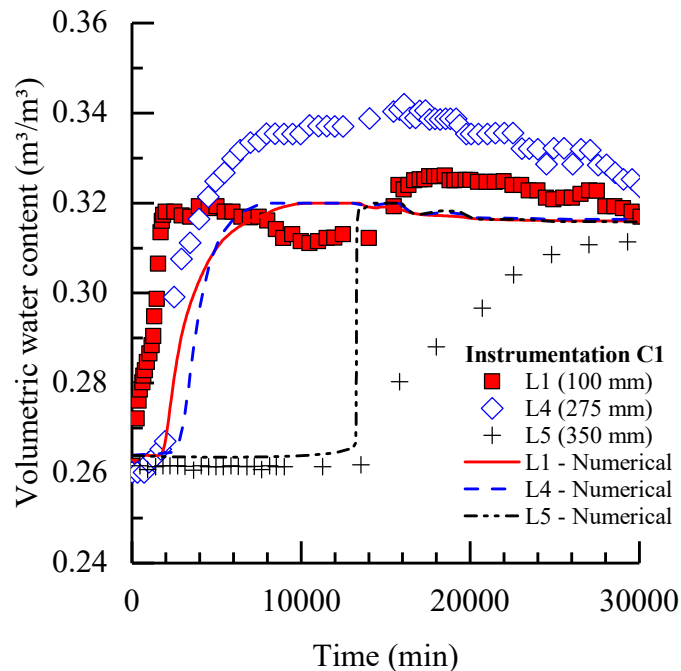
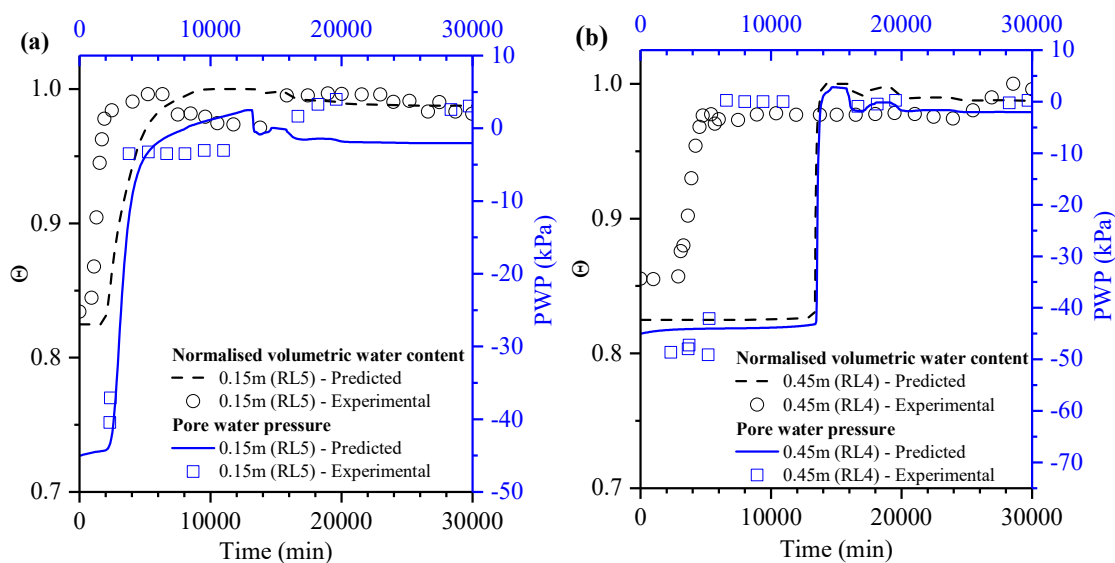


Figure 2.6 - Comparison of measured and numerically predicted results of wetting front during capillary barrier effect at instrumented column C1

Figure 2.7 presents a comparison of experimental and numerical PWP and volumetric water content data along the elevation of the full-scale wall. For the purposes of discussion of the results, negative PWP will be used to refer to matric suction. Measured and numerical values for PWP and volumetric water content for each reinforcement layer (RL1 to RL5) are shown, and data from the mid-height of each layer were compared. The numerical predictions were found to be reasonably consistent with the experimental measurements, thus validating the numerical model. Overall, better agreement was found between PWP values and the numerical predictions than between the volumetric water content measurements during soil during infiltration and the corresponding numerical predictions. Figure 2.7a shows good agreement for both volumetric water content and PWP changes during infiltration. The infiltration time history captured by the volumetric water content sensor located in RL4 (Figure 2.7b) appeared to be higher for the full-scale wall than the numerical predictions. This discrepancy between experimental and numerical data in RL4 is attributed to the three-dimensional nature of large-scale experiment, which is being simulated using a two-dimensional formulation. Water breakthrough at the soil-geotextile interface was found to occur non-uniformly along the nonwoven geotextile and to advance to the location of sensors in RL4 faster than expected. RL3 (Figure

2.7c) exhibited similar behavior as that observed in RL4, as the volumetric water content sensor (FDR) registered the presence of water sooner than expected. However, the PWP results predicted from the numerical simulations agree well with the measured PWP in the full-scale wall. In this case, the infiltration predicted using a two-dimensional numerical simulation was found to yield similar results to those monitored in the three-dimensional physical model of a geotextile-reinforced wall. It is possible that the time history of the advancing moisture front is more accurately portrayed by the data monitored by the tensiometers than by the moisture sensors (FDR). This is because while the tensiometers reflect the suction at a specific location, the FDR reflects the moisture content in a comparatively larger region of influence.

The experimental results presented in Figure 2.7d show that the initial normalized volumetric water content agreed well with the numerical initial conditions, with only a 2% difference observed. A delay of approximately 7,500 minutes between the numerical predictions and measured results was observed in RL2. Compaction heterogeneity and non-uniform infiltration in the physical model can explain these differences. The results obtained in RL1, shown in Figure 2.7e, show similar trends as those observed in RL2 (Figure 2.7d). The initial PWP was below the expected value, but the time required for water to reach the tensiometer during the experiment was similar to the value predicted in the numerical analysis. Consequently, the numerical simulation showed a consistent prediction of the infiltration time history based on the time history measured with the tensiometer readings.



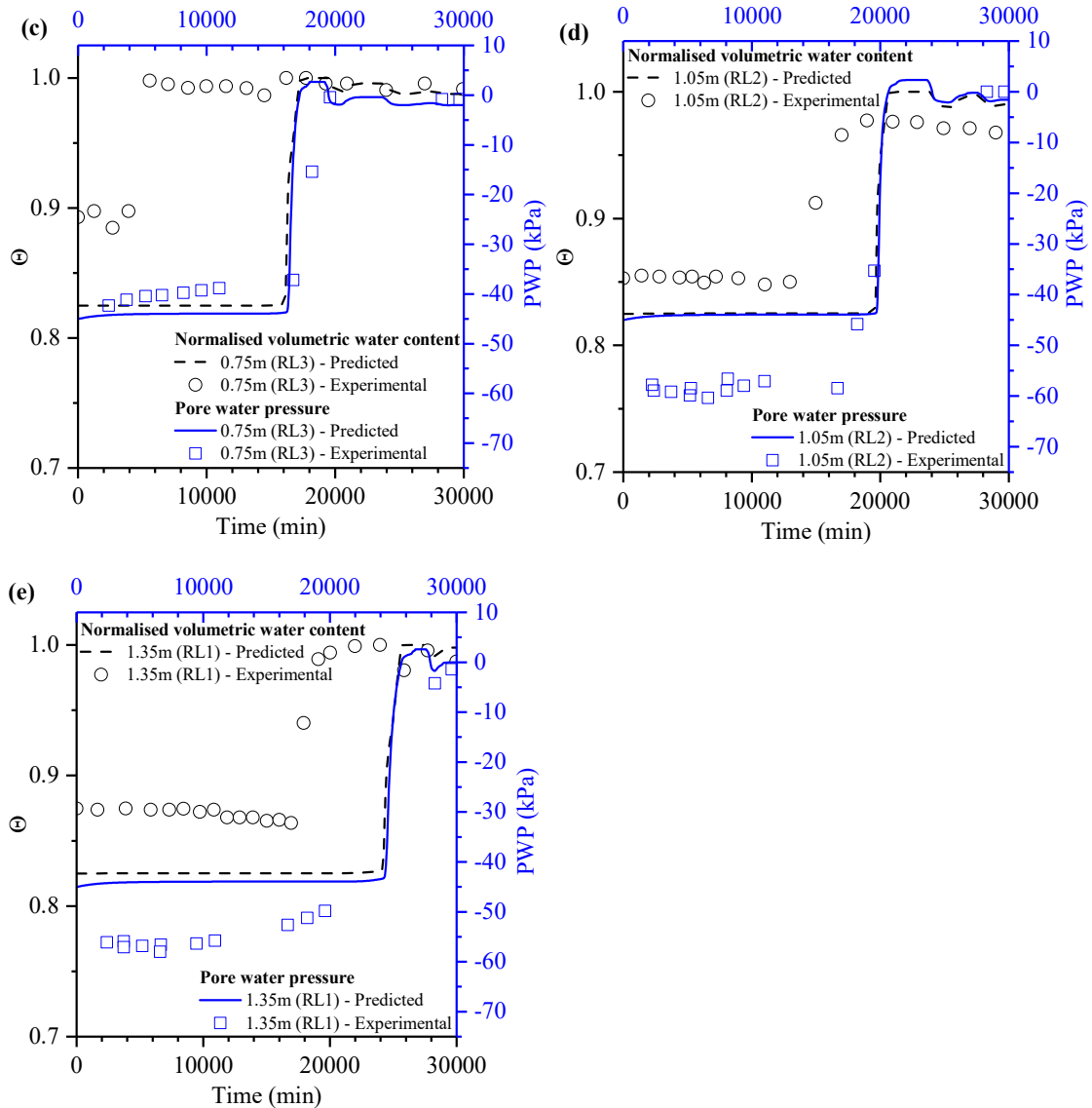


Figure 2.7 - Comparison of experimental and numerical changes in PWP and volumetric water content at different reinforcement layers (RL): (a) RL5; (b) RL4; (c) RL3; (d) RL2; (e) RL1

Because the time history of the tensiometer readings was deemed to be more accurate than that of the moisture content sensors, as illustrated by the results presented in Figure 2.7, the following numerical study of infiltration over time will be presented in terms of PWP.

## 2.6 Use of numerical simulation to extend interpretation of infiltration process into non-instrumented zones of the reinforced soil wall

Comprehensive monitoring of a large-scale experimental program using dense array of instruments throughout the entire geotechnical structure can be cost-prohibitive and timing consuming. In this context, numerical simulations can be helpful

by extending, after numerical calibration, the information gathered in instrumented zones into the non-instrumented zones of the geotechnical structure. The information presented in this section examines the impact of infiltration into non-instrumented zones of the geotextile-reinforced wall using the results of numerical simulations conducted after calibration of the numerical model using the previously evaluated monitoring data. Focus of the additional evaluation is on: the water infiltration near the secondary reinforcements resulting from wrap-around facing, the water infiltration near the wall face, the presence of comparatively less saturated regions within the reinforced wall, and the quantification of water volumes drained during infiltration to assess the efficiency of drainage geocomposites. Figure 2.8 displays the locations of vertical and horizontal sections defined as part of this study to refer to the profiles where the numerical results are presented next.

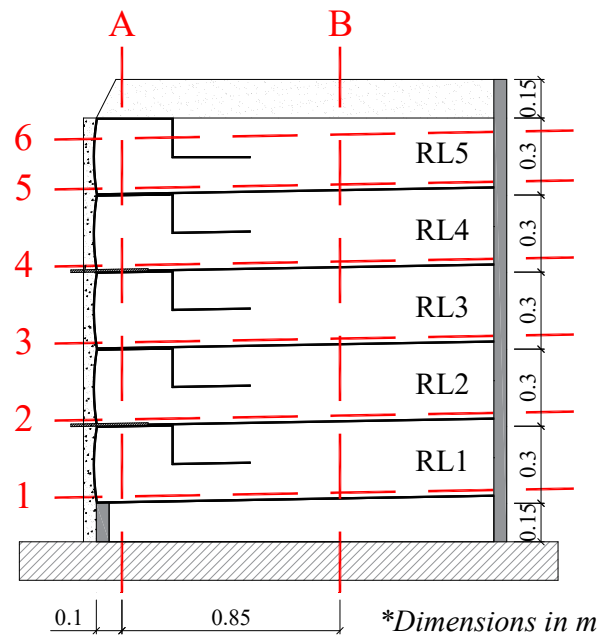
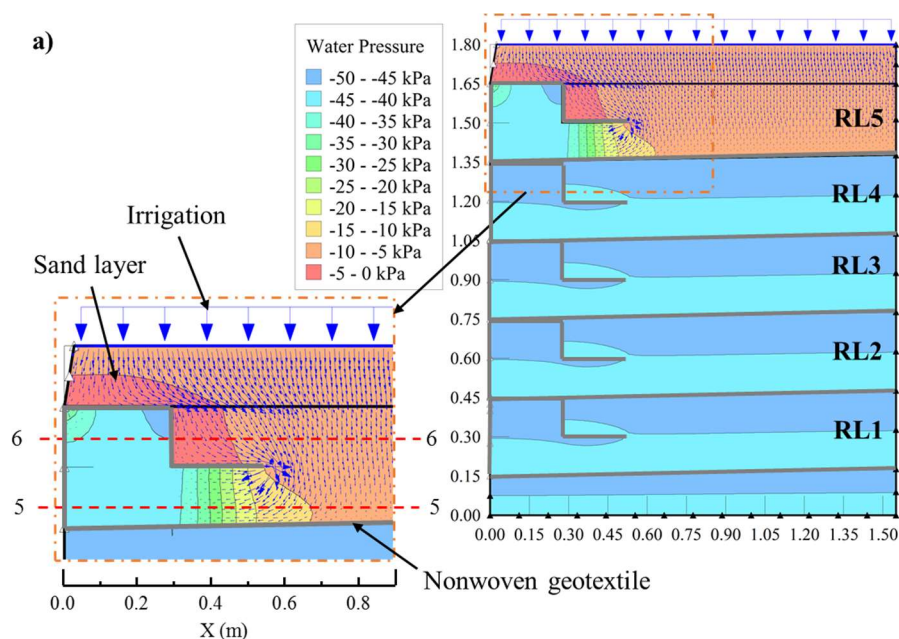


Figure 2.8 - Horizontal sections (1 through 6) and vertical sections (A and B) defined in the reinforced soil wall

## 2.7 Water infiltration near the secondary reinforcements resulting from wrap-around facing

Figure 2.9a provides the results of the numerical simulation conducted to assess the response of water infiltration near the secondary reinforcements that result as part of the wrap-around facing in the geotextile-reinforced wall. Specifically, the results in the figure correspond to a time of 5,000 min after initiation of the water infiltration. They indicate that the presence of secondary reinforcements between the primary

reinforcement layers changed the pattern of water flow. The results of the numerical simulation indicate that water flows through the nonwoven geotextile secondary reinforcements, saturating the soil in the vicinity of the wall face both over the top primary reinforcement and the top secondary reinforcement. On the other hand, water was observed to flow in a predominantly vertical direction over the zone of the reinforced wall beyond the length of the secondary reinforcements. Figure 2.9b shows the horizontal profile of PWP along Sections 6-6 and 5-5 (indicated in Figure 2.9a). After 5,000 minutes, Section 6-6 showed a significant change in PWP over a short distance, due to the presence of the geotextiles acting as secondary reinforcements. The presence of geotextile secondary reinforcements, which act as horizontal barrier to water flow, tend to maintain a comparatively high suction within the soil near the wall face. On the other hand, the PWP immediately above the top primary and top secondary reinforcements reached approximately -5 kPa. In contrast, cross section 5-5 showed a continuous decrease in PWP toward the wall face, indicating the development of a flow path with water moving toward the wall face. The numerical predictions presented in Figure 2.9b for 6,500 minutes shows that the sudden change in PWP, observed in cross section 5-5 at 5,000 minutes, becomes less significant, showing more gentle suction gradients and consequently less water migration toward the wall face. Eventually, after 8,000 minutes the moment where, the PWP profiles of 6-6 and 5-5 become essentially identical and with negligible gradient towards the wall facing.



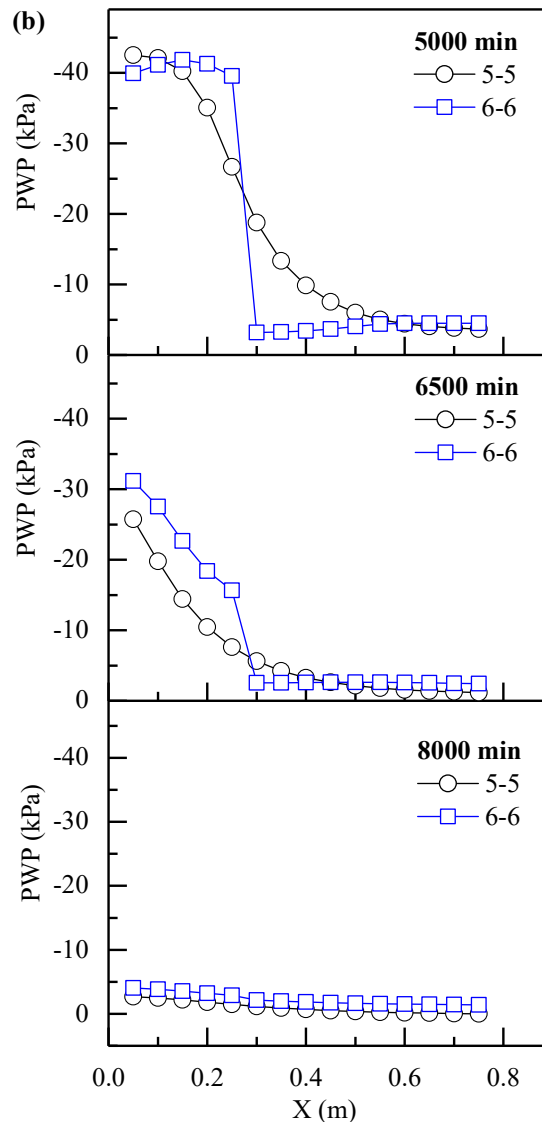
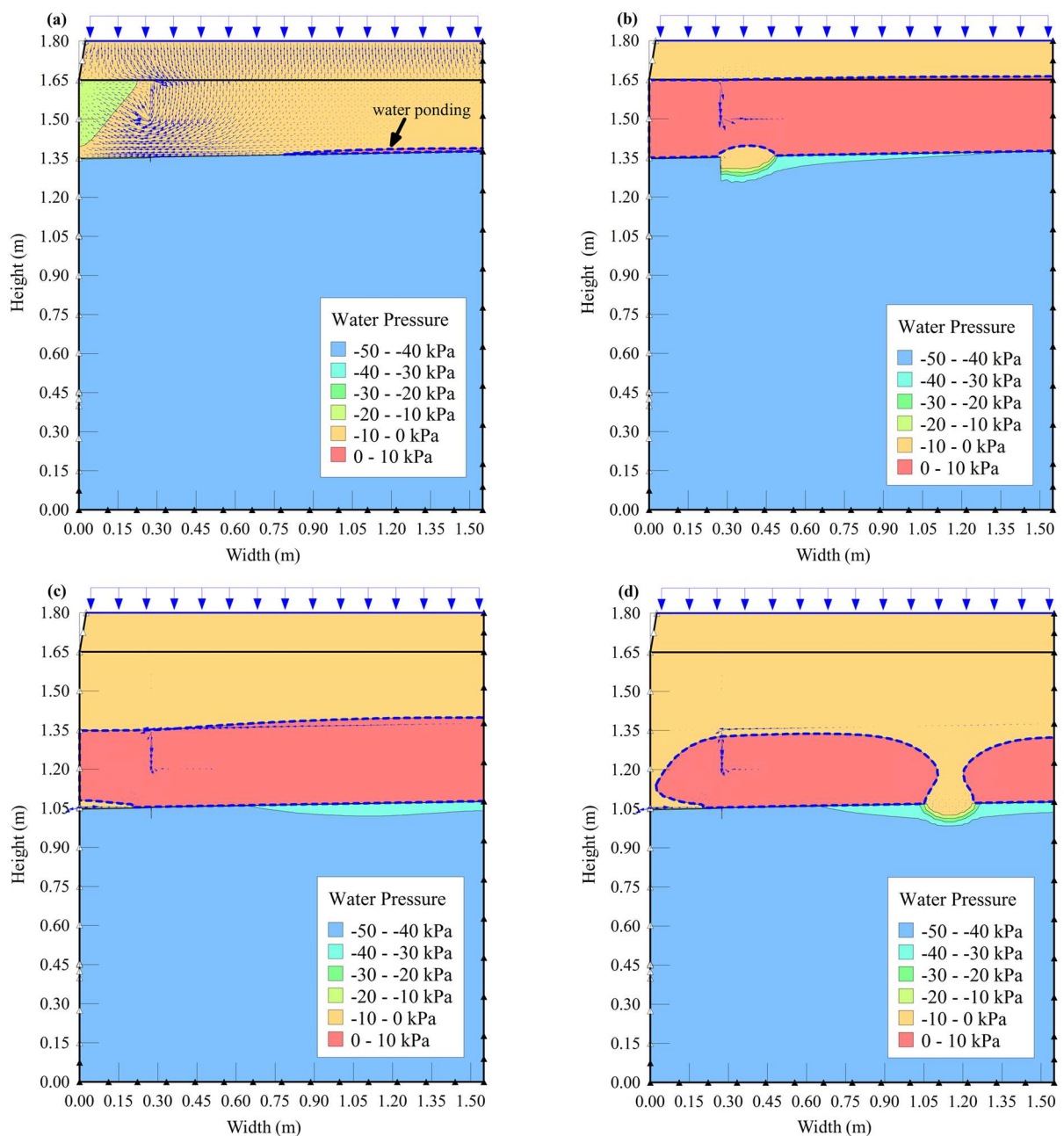


Figure 2.9 - Evaluation of infiltration near secondary reinforcements: (a) PWP contour lines at 5,000 min after infiltration; (b) change in PWP along cross section 6-6 and 5-5 at 5,000, 6,500 and 8,000 min following start of irrigation

## 2.8 Development of capillary barriers and generation of positive pore water pressures

After five days (7,416 minutes) of continued irrigation, water ponding occurred over geotextile RL5, as shown in Figure 2.10a, and water breakthrough was found to occur after 5,800 minutes (four days) later, as shown in Figure 2.10b. The infiltration front reached RL5 after approximately nine days (13,166 minutes). The results in Figure 2.10b also indicate that the soil layer over RL5 was fully saturated by the time that breakthrough of RL5 occurred, which explains the moistened shotcrete face near RL5, shown in Figure 2.11. The results of the numerical simulation indicate that water breakthrough occurred near the geotextile secondary reinforcement. Figure 2.10c and Figure 2.10d show the development of positive pore water pressures (ponded water)

on top of RL4 and the location where water breakthrough occurred, respectively. Water breakthrough at RL4 can be observed to occur toward the back of the reinforced soil wall (Figure 2.10d), as opposed to RL5, where water breakthrough occurred near the face of the reinforced soil wall (Figure 2.10b). The height of ponded water, which is higher towards the back of the wall, is consistent with the location where the breakthrough of water occurred (Figure 2.10c). Water breakthrough and the height of ponded water in RL3 and RL2 exhibited behavior similar to that observed in RL4. Figure 2.10e illustrates that when a steady state condition was eventually reached (30,000 minutes), ponded water can be observed to occur at the base of the wall.



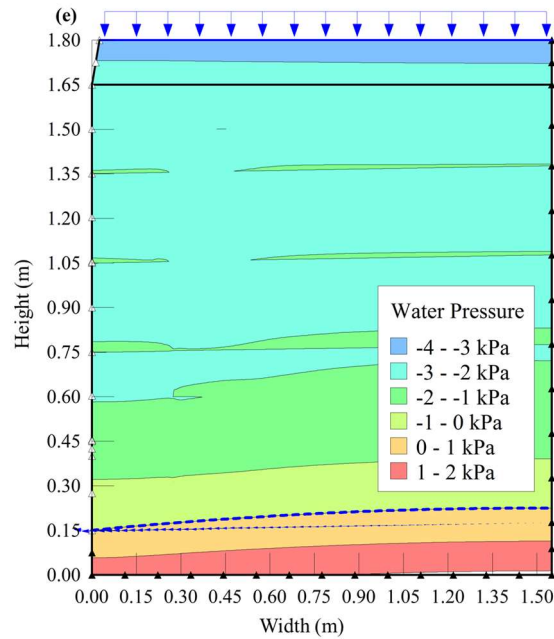


Figure 2.10 - Evaluation of the development of capillary barriers: (a) Ponding of water on top of RL5 (7,400 min); (b) breakthrough at RL5 (13,200 min); (c) ponding of water before water breakthrough at RL4 (15,780 min); (d) breakthrough at RL4 (15,800 min); (e) steady state condition (30,000 min)

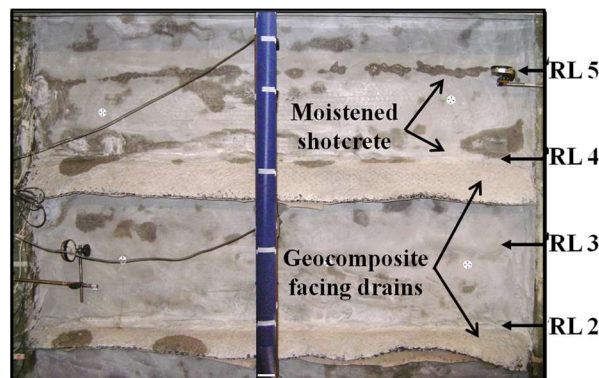


Figure 2.11 - Moistened shotcrete facing at end of experiment  
Source: adapted from Portelinha and Zornberg (2017)

## 2.9 Location of water breakthrough

The results in Figure 2.12 show the PWP along RL5 at times immediately before and after water breakthrough. The trend of PWP results in the figure illustrate that breakthrough at RL5 occurred near the wall face. After 10 hours of breakthrough of water (13791 min), PWP values were found not equilibrated along the geotextile length due to water advancing and starting to accumulate along the geotextile length at RL4. Additionally, a comparison of PWP along RL5 at 13,791 and 30,000 minutes (Figure 2.12) indicates that a steady state condition had not been established 10 hours after water breakthrough at RL5. This was facilitated by the presence of the underlying

reinforcement layer (RL4), which impeded the steady advancement of infiltrating water after RL5 breakthrough, affecting the magnitude of PWP within the soil layers overlying RL4.

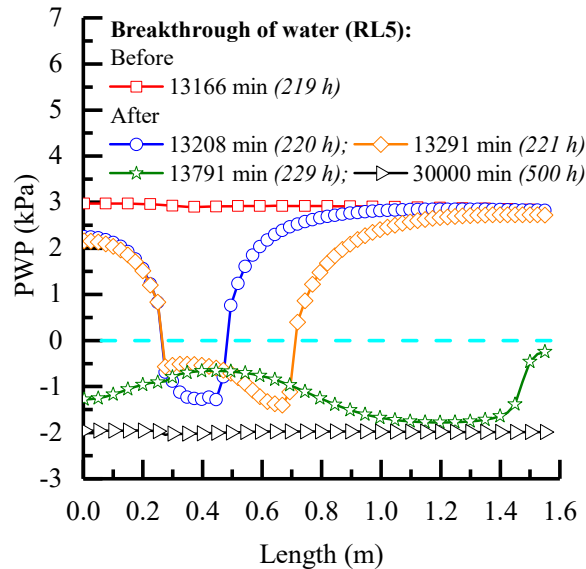


Figure 2.12 - PWP along RL5 before and after water breakthrough

A comparison of PWP along the reinforcement layers immediately following water breakthrough is shown in Figure 2.13. A substantial decrease in PWP was observed right after water breakthrough as a result of a rapid water advancement into the comparatively dry underlying soil layer. Water breakthrough at RL5 occurred near the wall face, mainly as a result of the influence of the hydraulic influence of the top secondary reinforcement. However, water breakthrough at RL4, RL3, RL2 and RL1 occurred towards the back of wall, which is consistent with the higher moisture accumulation expected at a comparatively long distance from the draining boundary. The magnitude of the decrease in PWP was observed to be similar in all reinforcement layers. Figure 2.13 also shows that drainage geocomposites controlled the increase in PWP at reinforcement interfaces, thus preventing development of positive PWP. Furthermore, a PWP up to 3kPa was observed in reinforcement layers in which no drainage geocomposites were installed.

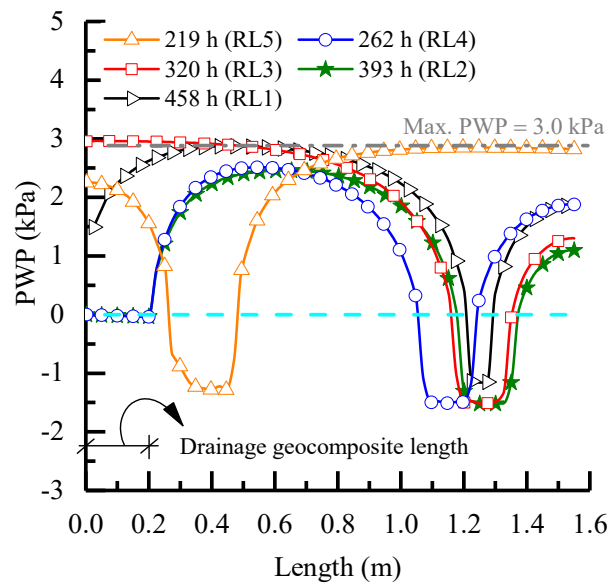


Figure 2.13 - Changes in PWP along reinforcement layers when water breakthrough occurred (cross sections 5 to 1, Figure 2.8)

## 2.10 Analysis of pore water pressure profiles

Figure 2.14a and Figure 2.14b show the PWP along vertical cross sections A and B, respectively. Along cross section A, a sudden change in PWP above RL5 (1.65 m) was observed at 7,416 minutes, whereas no such change was observed in cross section B. This difference is due to the presence of the nonwoven geotextile secondary reinforcement, which is intercepted by cross section A. A maximum PWP of 3 kPa above RL5 was observed at 13,166 minutes in both cross sections A and B. Figure 2.14a and Figure 2.14b also show that the capillary barrier effect occurred in every reinforcement layer as water advanced through the wall. Additionally, along cross section A, RL4 and RL2 maintained a maximum PWP of 0 kPa due to the presence of drainage geocomposites, while along cross section B, PWP development above RL4 and RL2 was similar to that observed for RL5, RL3 and RL1.

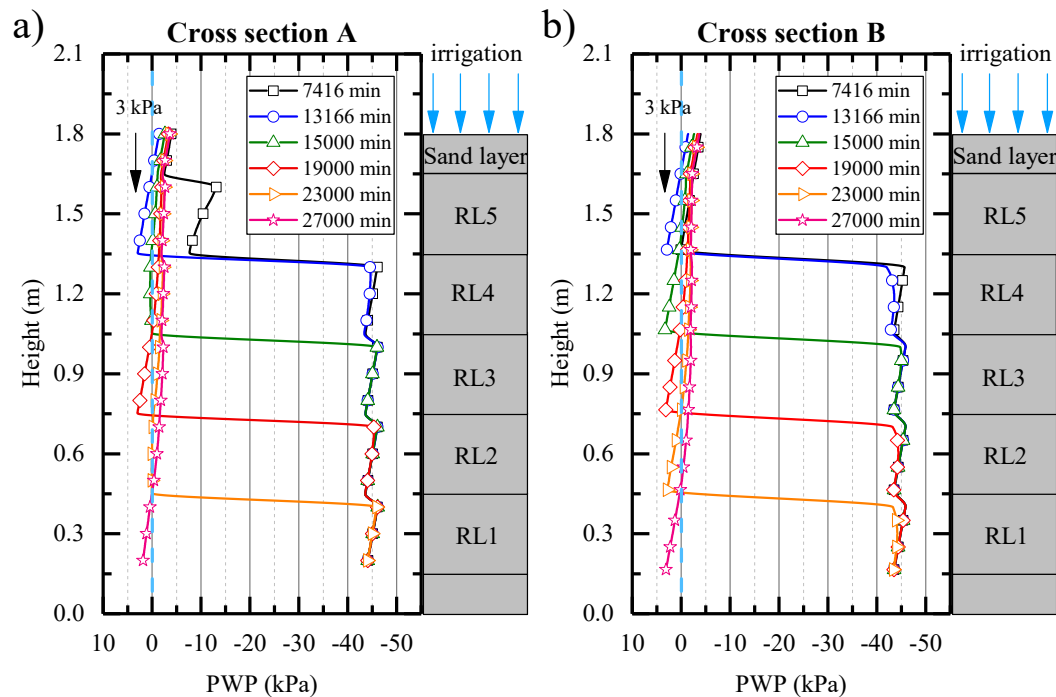


Figure 2.14 - Vertical profiles of PWP: (a) PWP along cross section A; (b) PWP along cross section B

## 2.11 Pore water pressure development at geotextile interface

Figure 2.15a shows the PWP along cross section A at the elevation of reinforcement layers RL1 to RL5 (Figure 2.8). Figure 2.15b shows the same information but for PWP ranging only from -5 kPa to +5 kPa. Figure 2.15b indicates that drainage geocomposites limited the PWP at RL4 and RL2 to a maximum of 0 kPa. In contrast, saturated conditions were maintained for 62 hours near the wall face. An increase of 1.5 kPa in RL5 was observed as water advanced into RL4, and a similar effect was observed in RL4, RL3 and RL2 as water ponded on top of RL3, RL2 and RL1, respectively. Additionally, Figure 2.15b shows a 3 kPa increase in PWP at the elevation of RL3, which was maintained for 23 hours. A less pronounced increase in pore water pressure was observed in RL1, which was registered approximately 2.5 kPa of PWP above geotextile interface. The presence of drainage geocomposites was observed to control the increase in PWP above the geotextile interfaces with RL4 and RL2, but the soil remained saturated for a longer time. Considering the effect of ponding water on adjacent reinforcement layers, RL4 remained saturated for 85 hours ( $\approx 3.5$  days) and RL2 for 95 hours ( $\approx 4$  days).

Figure 2.15c shows the PWP along cross section B at the elevation of reinforcement layers RL1 to RL5 (Figure 2.8). Also in this case, Figure 2.15d shows

the same information but for PWP ranging only from -5 kPa to +5kPa. The results in this figure show that water breakthrough at RL4 occurred 43 hours after water breakthrough at RL5, which was a much shorter timespan than the water advancement through RL5 (219.4 hours). This difference is consistent with the substantial amount of water ponded on top of RL5 (Figure 2.10b), causing a comparatively larger water flow into RL4 than the water influx applied on top of the wall. Water breakthrough at RL3, RL2 and RL1 was observed to occur 320, 393 and 458 hours, respectively, after the beginning of irrigation. The numerical results presented in Figure 2.15d show that water breakthrough in RL3, RL2 and RL1 occurred after approximately 58, 73 and 65 hours, respectively. Water breakthrough in RL2 (73 hours) took longer due to the presence of drainage geocomposites, which facilitated drainage through the wall face and regulated the length of time needed for water breakthrough to occur. Though drainage geocomposites were present in RL4, a comparable timespan was not observed, as the proximity of where irrigation was applied facilitated a faster buildup of PWP, as shown in Figure 2.15d. Additionally, Figure 2.15d indicates that a capillary break occurred when PWP on top of the nonwoven geotextile was approximately 3 kPa. As observed in the results presented in Figure 2.15b, the results presented in Figure 2.15d also reveal that water breakthrough at reinforcement layers affected the PWP of the overlying soil layers. Water breakthrough in RL3 affected the PWP of RL4, causing an increase of 2 kPa and a minor increase in RL5 as well. This increase in PWP in RL4, caused by ponding water on top of RL3, changed the soil-geotextile interface from an unsaturated to a saturated condition, and similar behavior was observed each time a capillary barrier break occurred and water ponded on top of the reinforcement layer.

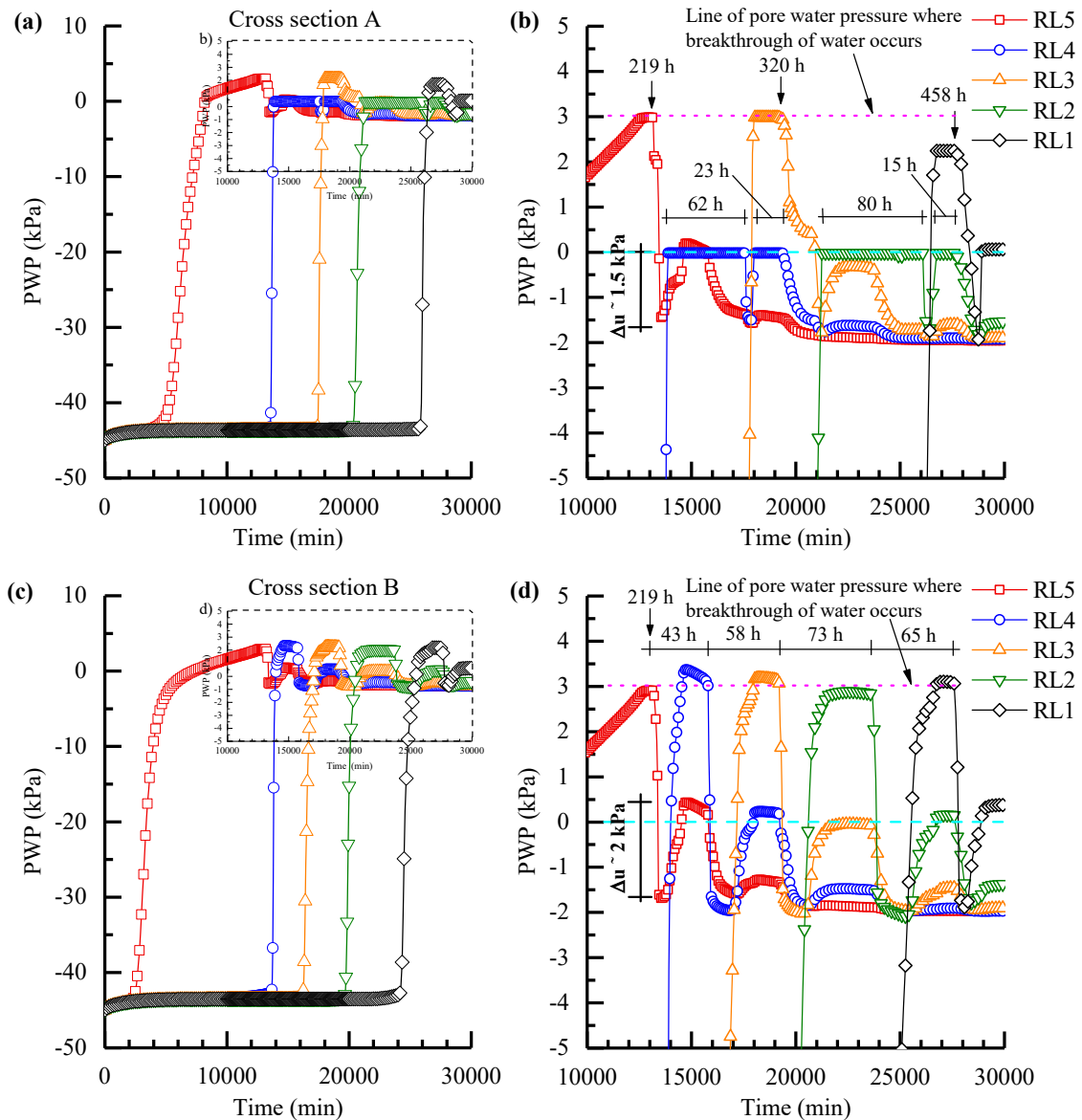


Figure 2.15 - Change in PWP along cross sections A and B at interfaces with RL5 to RL1: (a) cross section A, from beginning of numerical simulation; (b) zoom of predicted results from cross section A from 10,000 to 30,000 min; (c) cross section B, from beginning of numerical simulation; (d) zoom of predicted results from cross section B from 10,000 to 30,000 min

## 2.12 Cumulative water volume through different elements of the face

Although water was applied at a rate below the saturated hydraulic conductivity of the backfill soil, water could leave the reinforced soil mass (i.e. the domain of the numerical simulation) through the sand layer, shotcrete facing and drainage geocomposites. The cumulative water volume that drained from the domain in the numerical simulation is shown in Figure 2.16. Negative values indicate water leaving the domain. As expected, drainage geocomposites were found to provide a much larger flow capacity than the shotcrete facing. In addition, overflow through the top of

the reinforced soil mass (i.e. through the overlying sand layer) was observed to be higher than through the shotcrete facing, but the amount of water was considered negligible in comparison with the water drained through geocomposites. Approximately 72 L of water were drained over a period of 9.6 days. This is equivalent to 7.5 L per day or 30 drips per minute, considering a relatively low drip rate from the drainage geocomposites. Figure 2.16b presents the detailed cumulative water volume drained through the shotcrete facing and quantity of water overflow through the top (sand layer). The shotcrete facing drained approximately 0.037 L per day (37 ml/day), which was considered negligible and likely sufficient to moisten the shotcrete facing shown in Figure 2.11. The overflow through the top of the reinforced soil wall took 11 hours, resulting in an outflow of 9.37 L per day, equivalent to approximately 37 drips per minute.

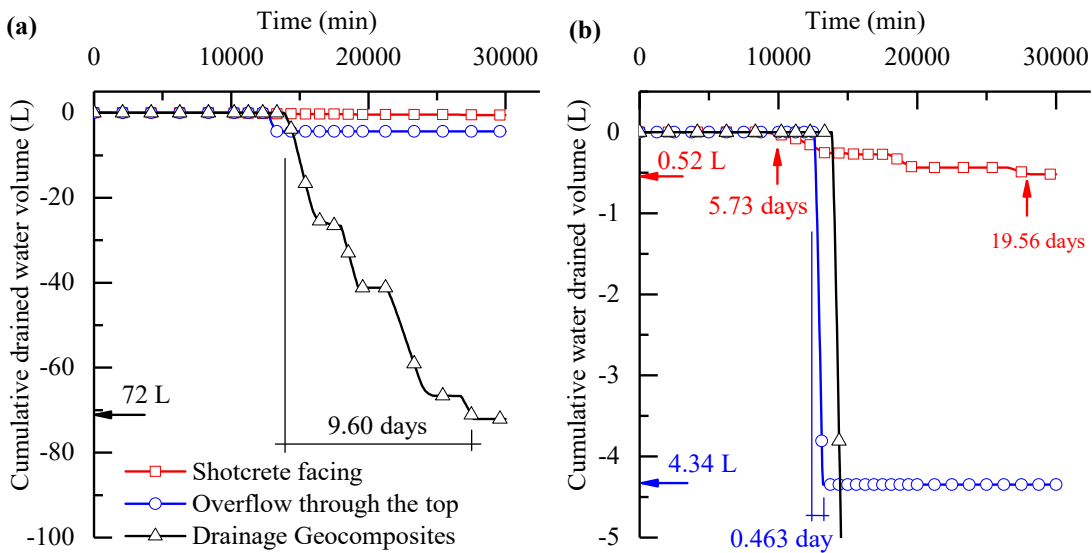


Figure 2.16 - Cumulative drained water volume from numerical analysis: (a) comparison of water drained through shotcrete facing, overflow through top and drainage geocomposites; (b) detailed drainage through shotcrete and overflow through top

Figure 2.17 shows the comparison of soil water storage, applied irrigation and water outflow. Changes in volumetric water content measured during the experiment were used to compute the soil water storage of each reinforcement layer. Experimental and numerical soil water storage into the reinforced soil wall agreed reasonably well. The experimental soil water storage showed a higher value than the applied irrigation during the first 10,000 min of simulation. This initial difference was attributed to the development of capillary barrier above the RL5 causing an increase in soil storage. Fig 17 also shows that these values above the applied irrigation agreed well with the

irrigation rate reported by Portelinha and Zornberg (2017). Though, as explained before, the simulations conducted using the reported irrigation rate (PORTELINHA; ZORNBERG, 2017) yielded large amounts of overflow that were not observed during the experiment. Therefore, the applied irrigation rate used in this study represented the infiltration process more accurately. Fig 17 also shows that approximately 13,000 min after infiltration began, the water outflow started to occur and, as a result, the applied irrigation diverged from the soil water storage. Essentially, the applied irrigation is equal to the change in soil water storage minus the water outflow which is clearly shown in Fig. 17. Overall, evaluation of the soil water storage and water outflow were considered to be consistent with the reduced inflow numerically simulated by irrigation through the top of the geosynthetic layer.

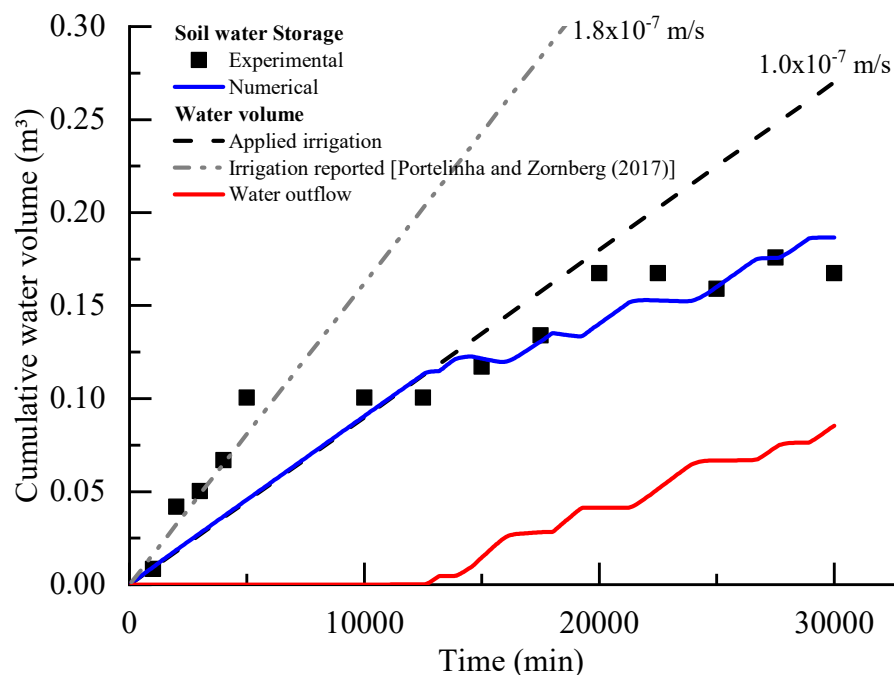


Figure 2.17 - Cumulative water volumes into the reinforced soil wall: soil water storage, applied irrigation and water outflow.

## 2.13 Conclusions

This chapter presents a numerical simulation of the infiltration processes involved in a large-scale laboratory geosynthetic-reinforced soil wall. The wall, reported in Portelinha and Zornberg (2017), was constructed using nonwoven geotextile reinforcements to facilitate internal drainage through the comparatively fine-grained soil mass. Soil and geosynthetic water retention curves were generated using laboratory data and calibrated to optimize the comparison between numerical

predictions and experimental results. The numerical simulations allowed evaluation of comparatively complex flow processes that could not be fully captured using only monitoring data. This included evaluation of the water flow pattern near the reinforcement anchorage, the location of water breakthrough, the development of capillary barriers and the effectiveness of drainage geocomposites. The following conclusions can be drawn from the numerical simulations and instrumentation data presented in this study:

- Comparison of numerical and experimental normalized volumetric water content indicates that initial saturation and initial void ratio changed along the height of the experiment.
- A numerical calibration using two measured variables (pore water pressure and volumetric water content) from the large-scale model provided more information than one measured variable was able to demonstrate. Results indicate that water breakthrough occurred non-uniformly across the nonwoven geotextile plane. Discrepancies between numerical and experimental results were attributed to the three-dimensional nature of the experiment. These observations indicate that any problem involving capillary barriers should be investigated using two field/experimental measured variables.
- The presence of geotextile secondary reinforcements was observed to trigger lateral water flow within the compacted soil layer, unlike the primarily vertical flow observed without the presence of secondary reinforcements.
- Ponding water, as a result of the development of capillary barriers over the geotextile reinforcements, was found to significantly increase PWP in the soil layer overlying each geotextile. Indeed, the development of capillary barriers yield positive pore water pressures in the vicinity of the geotextile interfaces.
- Water breakthrough in the top reinforcement layer was predicted to occur near the wall face, and away from the face (near the back of the wall) for subjacent reinforcement layers.
- The presence of drainage geocomposites on top of the nonwoven geotextile was found to locally control the development of positive PWP.

- Compared with the drainage geocomposites placed above reinforcement layers, the water drainage capacity of the shotcrete facing was found to be negligible. Additionally, the presence of a shotcrete facing prevented water from flowing through the face, causing water to pond on top of the reinforced soil structure.

Overall, the numerical predictions and monitoring results presented in this study indicate that the use of geotextiles with in-plane drainage capabilities allows internal lateral flow. However, geotextile reinforcements were found to develop a capillary break, leading to the development of positive pore water pressures in the soil overlying the reinforcements.



### **3. NUMERICAL SIMULATION OF INFILTRATION GEOTEXTILE-REINFORCED SOIL WALL CONSIDERING SOIL-ATMOSPHERE INTERACTION**

#### **Abstract**

This chapter presents a numerical methodology to consider soil-atmosphere interaction applied to infiltration into a geosynthetic-reinforced soil wall and its effect on wall stability. A hypothetical nonwoven geotextile reinforced soil wall was submitted to simulated conditions of evaporation and precipitation over 2 years considering local climate variation in São Paulo city, Brazil. Net infiltration and actual evaporation were quantified inside and outside of the reinforced zone allowing the assessment of changes in soil suction and factors of safety. The study discusses the implications of using in-plane draining reinforcements (e.g. nonwoven geotextiles) and soil-atmosphere effects. Results show that soil suction and factors of safety variation are more dependent of consecutive days of precipitation than isolated heavy rainfalls. For the climate conditions considered in this study, results showed that approximately 50% of the precipitation and potential evaporation turned into net infiltration and actual evaporation, respectively. Additionally, the numerical results revealed that after first wetting of the soil inside the reinforced soil zone, atmosphere demand for evaporation did not remove water from inside of the geosynthetic reinforced wall because of the capillary break.

#### **3.1 Introduction**

The performance of reinforced soil wall during rainfall conditions has been a concern in different regions around the world. In current practice, reinforced soil structures stability has been frequently analyzed not considering the unsaturated soil condition, but assuming the soil fully saturated overestimating the design. In unsaturated reinforced structures, the maintenance of the unsaturated condition is uncertain when subjected to precipitation-evaporation cycles. In this sense, the assessment of pore water pressures in unsaturated soil inside the reinforced zone during rainfall periods is necessary and complex, mainly when soil-atmosphere effects are considered in design analyzes.

Experimental and numerical studies involving the behavior of geosynthetic reinforced soil structures under real climate conditions are scarce. In general, studies

neglect the evaporation effect. Garcia, Gallage and Uchimura (2007) evaluated the performance of small-scale models of embankments reinforced with nonwoven geotextiles subjected to wetting and drying cycles. The models were 0.6 m high with two reinforcement layers spaced by 0.3 m. The embankments were subjected to wetting and drying cycles to observe the changes in pore water pressure (PWP) during and after rainfall events. Although evaporation occurred during the drying process (i.e. after rainfall), its value was not measured and considered during the analysis. Results showed that after rainfall (drying process) the soil suction below geotextile recovered much faster than above it. This indicates that after rainfall the capillary barrier was reestablished, and water accumulated above the geotextile was prevented of advancing deeper into the slope. Additionally, results show suction increases and volumetric water content reduction after rainfall indicating evaporation effects. Also, results showed that water accumulates over the nonwoven geotextile during rainfall and consequent local failure was observed at the proximity of embankment facing. The authors also evidenced increases of water content and pore water pressure of soil during the infiltration process. These increases were identified to occur because of the capillary break at the soil-geotextile interface. The development of capillary barrier between soil and nonwoven geotextile was experimentally and numerically evidenced in many published studies (STORMONT; MORRIS, 2000; IRYO; ROWE, 2004, 2005a; MCCARTNEY; ZORNBERG, 2010; THUO et al., 2015; PORTELINHA; ZORNBERG, 2017; LIMA et al., 2018). The basic concept of capillary barriers consists of small porous over a large porous material under unsaturated condition and with contrasting hydraulic properties. Therefore, in order to water move from the small porous material to the large one, the matric suction needs to reduce considerable to a point where breakthrough of water occurs (MORRIS; STORMONT, 1999; BATHURST et al., 2007; THUO et al., 2015; PORTELINHA; ZORNBERG, 2017; YANG et al., 2018).

Portelinha, Zornberg and Pimentel (2014) reported the performance of two instrumented sections of a geosynthetic-reinforced wall, one section was constructed with woven geotextile (no in-plane drainage) and the other with nonwoven geotextile (with in-plane drainage). The reinforced wall was 5.6 m high and fine-grained soil was used as backfill. Construction occurred during the summer in Brazil (wetting season) and, as a result, the reinforced wall was subjected to rainfall during construction. Monitoring program was carried out for a period of one year. Reinforcement

displacements were monitored in both sections. Major displacements were observed to occur during construction. The performance of the nonwoven geotextile section was reported to be equivalent to the behavior of the woven geotextile section. Changes in suction during rainy and non-rainy periods was monitored using tensiometers only in the nonwoven section. During construction the reinforced soil wall experienced to a total of 490 mm of cumulative rainfall over 18 days. Results show that these rainfall events caused a significant reduction in suction to approximately 15 kPa and 20 kPa at the sensors located at the bottom of the wall and at the unreinforced embankment, respectively. Tensiometer readings show that, for most monitored layers, soil suction reaches a minimum value of 5 kPa, except for the bottom reinforcement layer where soil suction was observed close to 0 kPa. Also, results show increases of suction in all sensors along the height of the reinforced soil wall during the drying months, evidencing evaporation effects.

In literature, studies that reported the effect of climatic changes involving precipitation-evaporation cycles were conducted to unreinforced slopes (GASMO et al., 2000; GRIFFITHS; LU, 2005; TAKE; BOLTON, 2011; YANG et al., 2017).

Gasmo, Rahardjo and Leong (2000) evaluated the stability of a monitored slope of silty clay subjected to climatic changes. Numerical simulations of infiltration were performed to investigate pore water pressure behavior over time. The authors applied infiltration and evaporation for an unspecified duration to simulate the measured initial pore water pressure in the model. After matching field and numerical initial pore water pressure, numerical simulations of infiltration and stability analysis were conducted considering the unsaturated soil strength. Results showed that water infiltration in the field occurred faster than in the numerical modeling with hydraulic parameters determined in laboratory. The authors discussed that the triaxial permeameter used to determine soil saturated permeability required a minimum of 10 kPa of effective confining pressure which probably avoided the cracks and fissures existents in the samples. Despite of differences between numerical and field values of pore water pressures, the authors observed that infiltration caused rapid reduction in factor of safety over short periods. On the other hand, the factor of safety was observed to increase slowly due to evaporation.

Griffiths and Lu (2005) also evaluated the stability of an unsaturated slope under steady infiltration and evaporation using finite element analysis. Similarly to Gasmu, Rahardjo and Leong (2000), the authors found that evaporation improved the stability of clayey slopes, while during infiltration the factor of safety diminishes. On the other hand, high evaporation rates reduced the factor of safety of silt slopes due to excessive drying of soil. Therefore, the improvement of stability due to suction changes were observed to be more significant in clayey slopes than in silty slopes.

Take and Bolton (2011) studied the behavior of instrumented kaolin clay slopes in centrifuge tests subjected to artificial climate variations. Infiltration and evaporation effects were simulated by changes on air relative humidity. In order to simulate infiltration effect, the air relative humidity was adjusted to 100%, while for evaporation its value was set to 40%. In order to simplify the analysis and assume the soil saturated, the authors controlled the maximum suction to be less than the air entry value. Pore water pressure changes were observed to occur faster during soil wetting than during drying. These experimental results agreed with the sudden variation of the factor of safety during wetting events observed by Gasmu, Rahardjo and Leong (2000). Additionally, the authors showed that seasonal climate conditions caused progressive soil softening due to moisture advancing leading to slope failure. Back analysis on centrifuge tests using the Spencer limit-equilibrium method indicated that, clay slopes that experience average stress higher than the critical state stress in any time of the year, may experience progressive failure due to seasonal variations of pore water pressure.

Yang *et al.* (2017) conducted back analysis of two slopes considering local climatic variation. One of the slopes collapsed due to a torrential rainfall event during the Typhoon Jangmi in 2008 and the other suffered large deformations caused by consecutive wetting and drying cycles. Rainfall events were applied as an hourly influx and evapotranspiration was considered as a daily average rate of 10 mm/day during dry days. For the slope that collapsed, meteorological data showed that during the typhoon approximately 500 mm of rainfall occurred in 3 days. Slope collapse occurred after 2 days of typhoon occurrence. Numerical results precisely simulated the slope failure after 48 hours of torrential rainfall. For the slope that experienced excessive deformation, the numerical model was able to properly predict the deformation with time considering the climatic changes in 2012. The authors concluded that the factor

of safety is mostly affected by accumulated rainfall than a heavy rainfall event. This finding suggest that hydrological data should be used to accurately assess stability under real climate conditions.

Although many studies have reported the effect of infiltration on reinforced and unreinforced soil structures stability or performance (IRYO; ROWE, 2005a; BHATTACHERJEE; VISWANADHAM, 2015; THUO et al., 2015; YANG et al., 2018), most of them were conducted considering critical precipitation for long periods. This methodology does not represent the actual climate condition throughout the operational period of the soil structure. The existing studies involving real climatic changes simulations were applied to unreinforced slopes. Differently from the previous studies, the present study was conducted to evaluate the stability of a geosynthetic-reinforced soil wall with simulation of actual climate condition. This study includes the water transfer at ground surface quantifying the net infiltration, surface runoff and actual evaporation. Also, the soil suction changes are evaluated together with the changes in factor of safety over 2 years of climatic changes. This study also investigate the soil suction changes before and after first wetting of the reinforced zone. Additionally, the implications of using nonwoven geotextiles, with in-plane drainage function, as reinforcements are presented.

## **3.2 Methodology to apply rainfall and evaporation**

### **3.2.1 Modelling of soil-atmosphere interaction**

The consideration of soil-atmosphere interaction is a complex problem to solve and depends on wind velocity, net radiation, precipitation, ground freezing, soil pore water pressure and local vegetation. In this study, the interaction between soil and atmosphere was conducted considering two atmospheric variables: precipitation and evaporation. Differently from precipitation, evaporation is variable that depends on wind velocity, net radiation and soil water content. While precipitation is variable that depends on air masses movement with contrasting temperature and moisture. Evaporation was assumed to occur only during non-rainy days.

In this study ground surface was assumed to have no vegetation and ground freezing was neglected in view of climate conditions in southeast of Brazil where temperatures are above freezing condition. The software SEEP/W (GEO-SLOPE,

2018a) was used to simulate both rainfall and evaporation using the land-climate interaction (LCI) boundary condition.

The software SEEP/W (GEO-SLOPE, 2018a) uses the following mass balance equation to calculate water flux at ground surface.

$$q_P \cos \alpha + q_E + q_R = q_I \quad (3.1)$$

where  $q$  is water flux due to rainfall ( $q_P$ ), evaporation ( $q_E$ ), runoff ( $q_R$ ) and infiltration ( $q_I$ );  $\alpha$  is the slope angle. In case of water infiltration result in positive pore water pressure (i.e. water ponding) at any superficial node, the pore water pressure was set to zero and runoff was computed using the following equation.

$$q_R = q_I^{\text{applied}} - q_P \cos \alpha - q_E \quad (3.2)$$

where  $q_I^{\text{applied}}$  is the applied infiltration flux. Daily rainfall used in the analysis were obtained from the Institute of Astronomy, Geophysics and Atmospheric Sciences of University of São Paulo (IAG-USP).

### 3.2.2 Simulation of actual evaporation

In this study, actual evaporation (AE) was computed using monthly potential evapotranspiration data from the Mirante de Santana station – São Paulo state, (OMM: 83781), National Institute of Meteorology of Brazil (INMET, Brazil). Potential evapotranspiration was considered to calculate actual evaporation as this parameter represent the water transfer from soil and vegetation to the atmosphere. For vegetation free consideration, the potential evapotranspiration was assumed as the potential evaporation (PE). According to Rianna, Pagano and Urciuoli (2014) the term “potential evaporation” refers to a condition in which soil water supply is not limiting, and evaporation occurs according to atmospheric demanding. The “actual evaporation” refers to a condition where soil water availability is limited, and evaporation rate is dependent of the soil unsaturated condition (i.e. water content and unsaturated hydraulic conductivity). Therefore, as soil desaturates, a gradual reduction of actual evaporation occurs leading to atmospheric demand for evaporation less satisfied.

In order to compute the daily actual evaporation, the relationship proposed by Wilson, Fredlund and Barbour (1997) was used.

$$q_{AE} = q_{PE} \left[ \frac{\exp\left(\frac{\psi g W_v}{RT}\right) - h_a}{1 - h_a} \right] \quad (3.3)$$

where  $q_{AE}$  is the actual evaporation,  $q_{PE}$  is the potential evapotranspiration,  $\psi$  is the matric suction,  $g$  is the acceleration,  $W_v$  is the molecular weight of water (0.018 kg/mol),  $R$  is the universal gas constant (8.314 J/(mol·K)),  $T$  is the absolute temperature (K), and  $h_a$  is the relative humidity of the air above soil. It should be noted that the previously equation proposed and verified by Wilson, Fredlund and Barbour (1997) assumes that air, water and soil have similar temperature. Daily temperature and relative air humidity used to compute actual evaporation were obtained from IAG-USP.

In this study, the applied evapotranspiration will be referred as applied evaporation in the results.

### 3.3 Climatic changes consideration

Analysis were performed using climate data from 2013 and 2014 of São Paulo city, Brazil. The precipitation during this period was similar to the historical annual average for the São Paulo city, Brazil. The historical average reported by the IAG-USP is from 1933 to 2017. Figure 3.1 shows the precipitation and evaporation regime considered in the annual analyses. It should be noted that evapotranspiration was constant over the year while precipitation considerably changed.

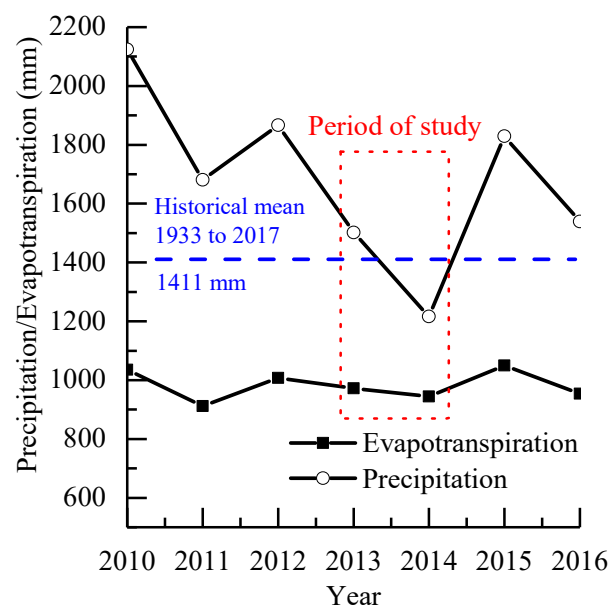


Figure 3.1 - Period of analyses for evaluation of climate change effects

Figure 3.2 illustrate the monthly precipitation, relative air humidity and temperature between 2013 and 2014 as adopted in numerical analyses. The figure shows that most rainfall events occurred during the spring and summer (wetting seasons) period that temperatures are the highest during the period. During autumn and winter (drying seasons), rainfall events and temperature reduced compared to spring and summer. Relative air humidity was observed to significantly varies during the winter and spring compared to summer and autumn.

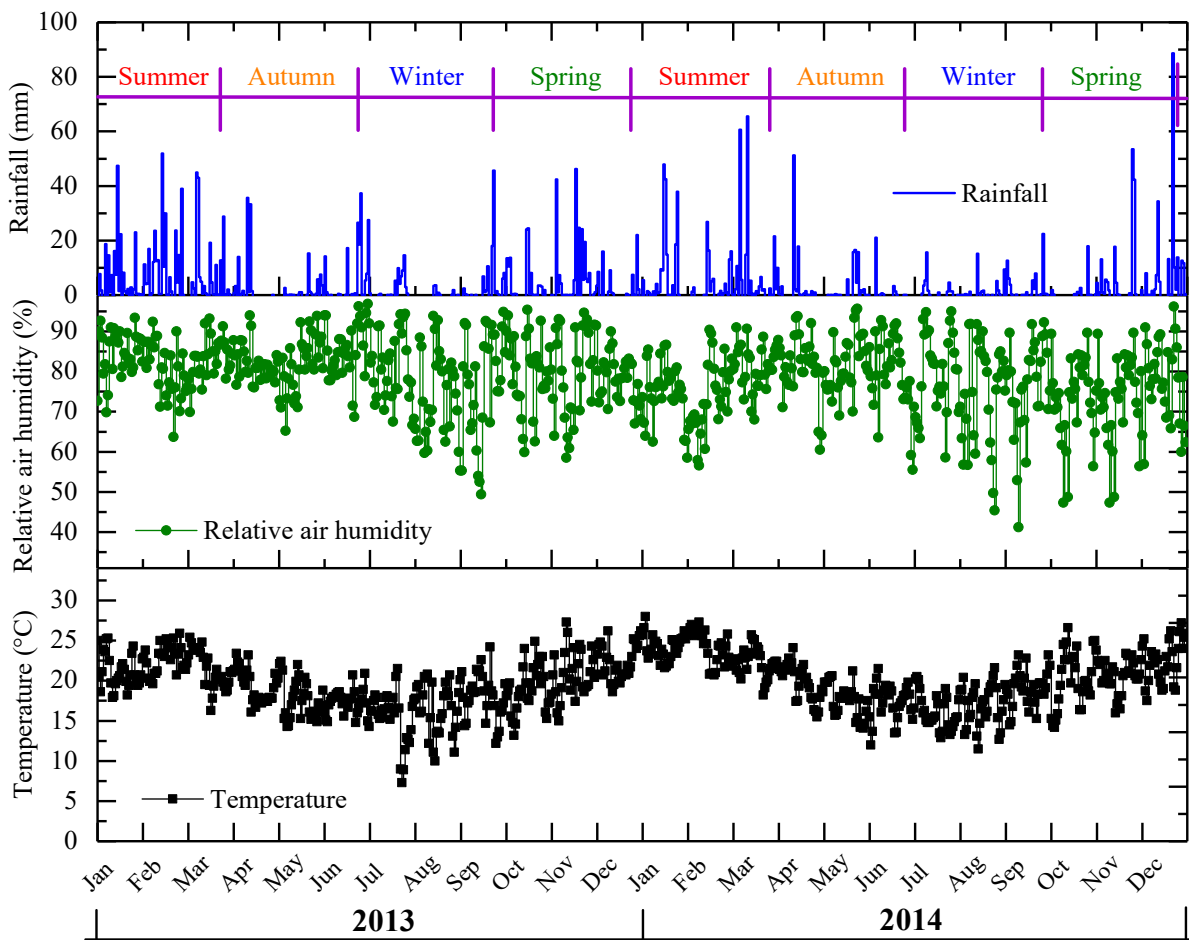


Figure 3.2 - Daily rainfall, relative humidity and temperature between 2013 and 2014

### 3.4 Numerical model of a GRS wall

#### 3.4.1 GRS wall section

Reinforcement spacing of the hypothetical GRS wall was determined following the guidelines of the Federal Highway Administration (BERG et al., 2009) which uses Rankine's theory. Final analyses resulted in a geotextile 4 m long and spaced every 0.4 m resulting in 11 reinforcement layers (with one embedded layer, see Figure 3.3). Wall face was designed with an inclination of 1H:10V. Three drainage geocomposites,



geotextile. Table 3.1 summarizes the index properties of the nonwoven geotextile. In the numerical modelling, both soil and geotextile were considered isotropic materials.

Table 3.1 - Characteristic properties of soil and geotextile

Material	Characteristics	Values
Backfill soil <sup>a</sup>	Clay fraction	32%
	Silt fraction	12%
	Sand fraction	56%
	Gs	2.75
	LL	40%
	PL	19%
	PI	21%
	$\gamma_d^{\max}$	17.9 kN/m <sup>3</sup>
	W <sub>opt</sub>	14.6%
	k <sub>sat</sub>	4.9 × 10 <sup>-7</sup> m/s
	Friction angle, $\phi'$ (°)	35
Cohesion, $c'$ (kPa)	0	
Nonwoven geotextile	Weight per unit area	500 g/m <sup>2</sup>
	Thickness	3.00 mm
	Permittivity	1.96 s <sup>-1</sup>
	Porosity	0.94
	Tensile strength	26 kN/m

<sup>a</sup> modified from Portelinha and Zornberg (2017) and Albino *et al.* (2018)

The hydraulic properties of the geotextile were modelled considering the water retention curves and hydraulic conductivity functions shown in Figure 3.4 and Figure 3.5, respectively. Soil and geotextile water retention curve (Figure 3.4) were obtained using back analysis based on volumetric water content (VWC) and pore water pressure (PWP) data from the laboratory test compared to numerical simulation results by Albino *et al.* (2018). Water retention curves hysteresis due to drying and wetting paths was neglected in this study. Although this assumption may lead to different results from those expected in field conditions, it is reasonable for soil-atmosphere evaluation in GRS walls. The complete consideration of SWRC hysteresis in numerical modelling is a complex problem because wetting and drying paths are expected to change based on the soil pore water pressure. Also, the numerical evaluation conducted in this study

assumed that the vapor transfer is neglectable in comparison to water transfer through the porous media.

The water retention curves of nonwoven geotextile and soil were modelled using the van Genuchten (1980) (Equation 3.4) and Durner (1994) (Equation 3.5) models, respectively. Durner (1994) model was used to accommodate the bimodal trend of the soil water content data. Fitting parameters of the water retention curve of both soil and geotextile are shown in Figure 3.4. Details of the procedure to define water retention curves can be found in the previous chapter.

$$\Theta = \frac{\theta - \theta_r}{\theta_s - \theta_r} = \left( \frac{1}{1 + (\alpha\psi)^n} \right)^m \quad (3.4)$$

$$\Theta = w_1 \left[ \frac{1}{1 + (\alpha_1\psi)^{n_1}} \right]^{m_1} + (1 - w_1) \left[ \frac{1}{1 + (\alpha_2\psi)^{n_2}} \right]^{m_2} \quad (3.5)$$

where  $\Theta$  is the normalized volumetric water content,  $w_1$  and  $w_2$  are the initial gravimetric water content of each segment of the bimodal curve;  $\psi$  is the matric suction;  $\theta_s$  is the saturated volumetric water content;  $\theta_r$  is the residual volumetric water content; and  $n$ ,  $m$  and  $\alpha$  are the curve fitting parameters.

The k-function (Figure 3.5) were obtained using Mualem (1976) (Equation 3.6), based on the water retention curves, as presented in Figure 3.4.

$$k = k_{sat} \Theta^{1/2} \left[ 1 - \left( 1 - \Theta^{1/m} \right)^m \right]^2 \quad (3.6)$$

where  $k$  is the hydraulic permeability.

The gravel surrounding the pipe at the back of the GRS wall was considered with a constant hydraulic conductivity as shown in Figure 3.5. Additionally, for the infiltration modelling the initial suction was assumed as 45 kPa based on Albino *et al.* (2018) as shown in Figure 3.5.

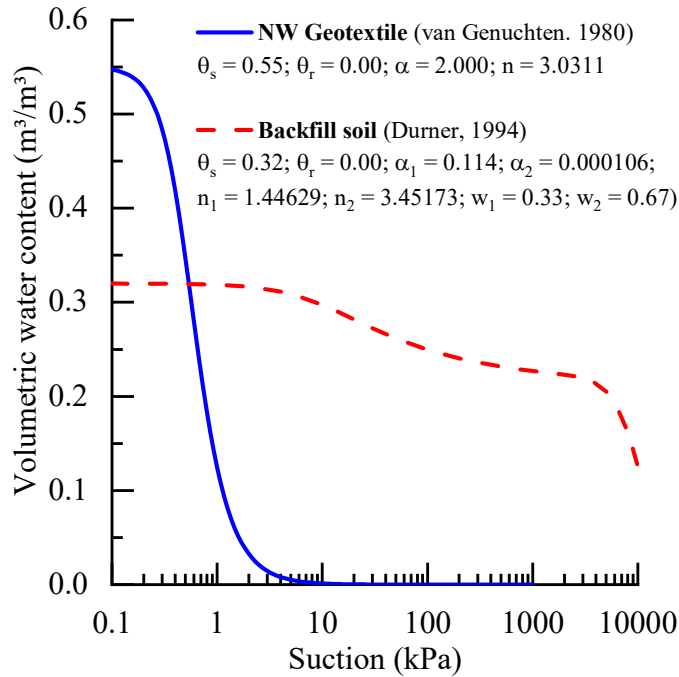


Figure 3.4 - Backfill and nonwoven geotextile water retention curves adopted from Albino *et al.* (2018)

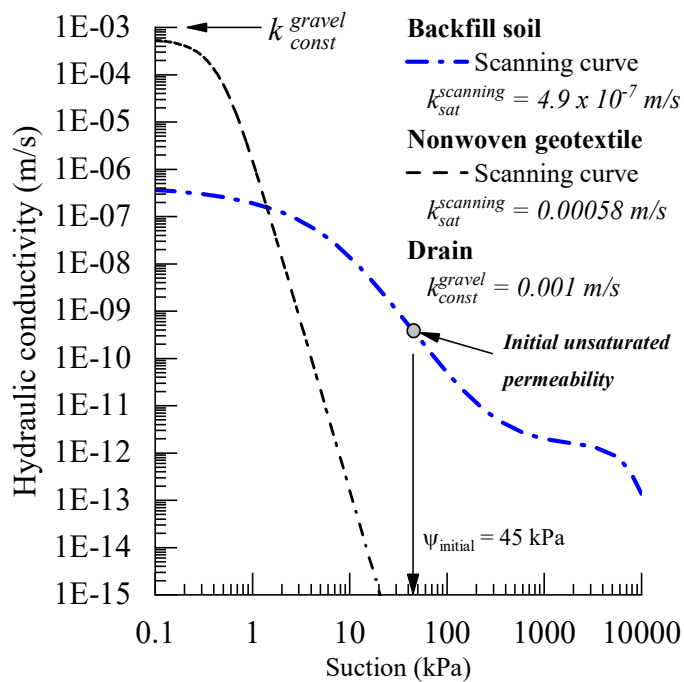


Figure 3.5 - Unsaturated hydraulic conductivity of soil and nonwoven geotextile

### 3.4.3 Infiltration modelling

The water climatic effects (i.e. infiltration and evaporation) on a hypothetical nonwoven geotextile reinforced soil wall with 4.0 m high was modelled with the Finite Element Method (FEM) using SEEP/W (GEO-SLOPE, 2018a). Figure 3.6 shows the numerical model mesh, dimensions and sections for pore water pressure observation.

The numerical model was constructed with a total of 13103 triangular elements and 7691 nodes. Nonwoven geotextile was modeled as a line element with hydraulic properties assigned across its thickness. The top of the reinforced wall, as well as, the reinforcements were modelled with a 1% inclination towards the wall face to facilitate drainage and prevent water ponding. The region of the model that comprehend the compacted soil is shown in Figure 3.6.

The observational sections A and B were positioned inside the reinforced zone and they were located 1 m and 2 m from wall face, respectively. Section C was positioned 7 m from wall face and outside of reinforced zone. Along section A, B and C, three horizontal section (i.e. section 1, 2 and 3) were located to create additional observational points shown as red circles.

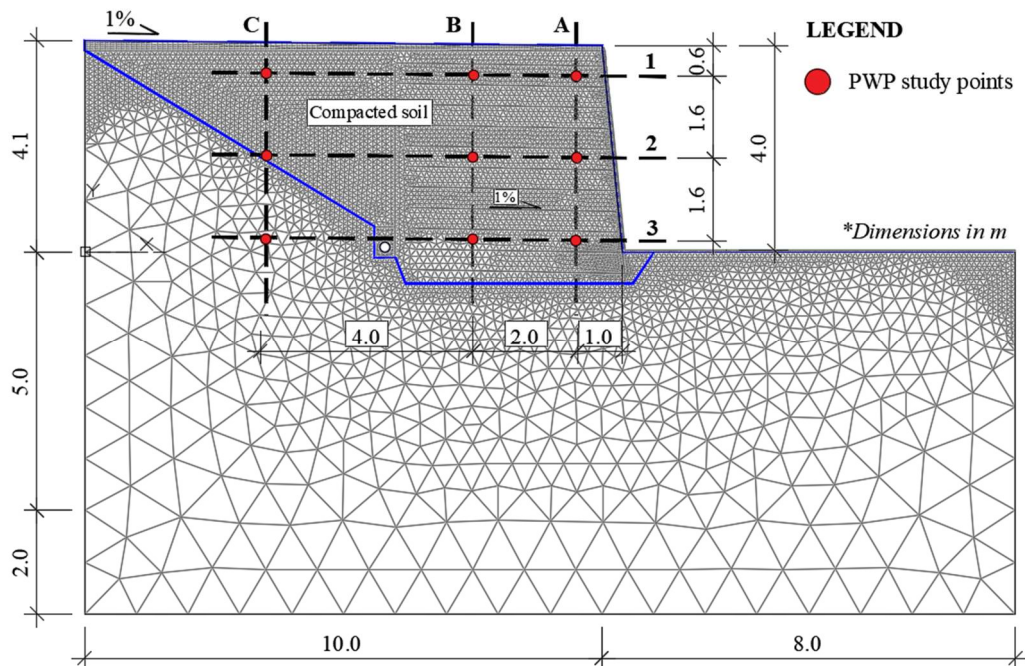


Figure 3.6 - Illustration of GRS model and observational sections

Figure 3.7 shows the boundary and climate conditions used in the GRS wall. A permeable boundary condition was adopted for the wall face and for the discharge pipe, where water was drained only in the case of pore water pressure became positive in any node. Upward and downward flow indicates evaporation and precipitation, respectively. Stationary ground water table at 7 m below wall toe was considered maintaining water pressure head to 0 m throughout the duration of the analysis. Initial pore water pressure of soil foundation (i.e. soil that was not compacted, see Figure 3.6) was defined considering capillary rising limited to 5 m (50 kPa) over the assumed

water table. Shotcrete facing and drainage geocomposites conductivity were assumed as based on Albino *et al.* (2018) as shown in Figure 3.7.

**LEGEND**

- **Boundary conditions**
  - △ Permeable boundary condition
    - $Q = 0 \text{ m}^3/\text{s}$  if  $h_p < 0$
    - $Q > 0 \text{ m}^3/\text{s}$  if  $h_p > 0$
- **Materials**
  - Shotcrete facing
    - Conductivity =  $1 \times 10^{-12} \text{ m/s}$
  - Drainage geocomposite
    - Tangential conductivity =  $0.0582 \text{ m/s}$
    - Normal Conductivity =  $0.0035 \text{ m/s}$
  - Nonwoven geotextile
    - Conductivity: See Figure 3.4
  - Gravel
    - Conductivity:  $0.001 \text{ m/s}$

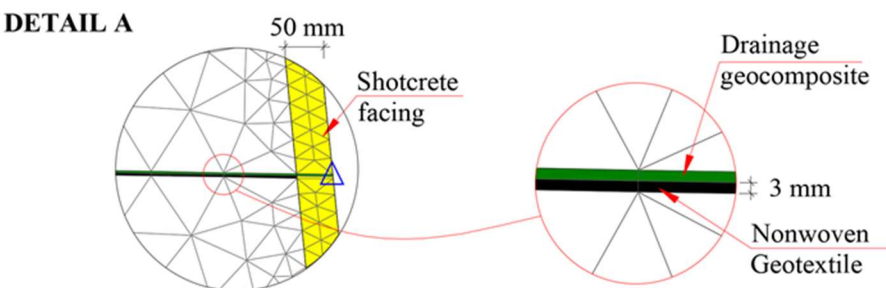
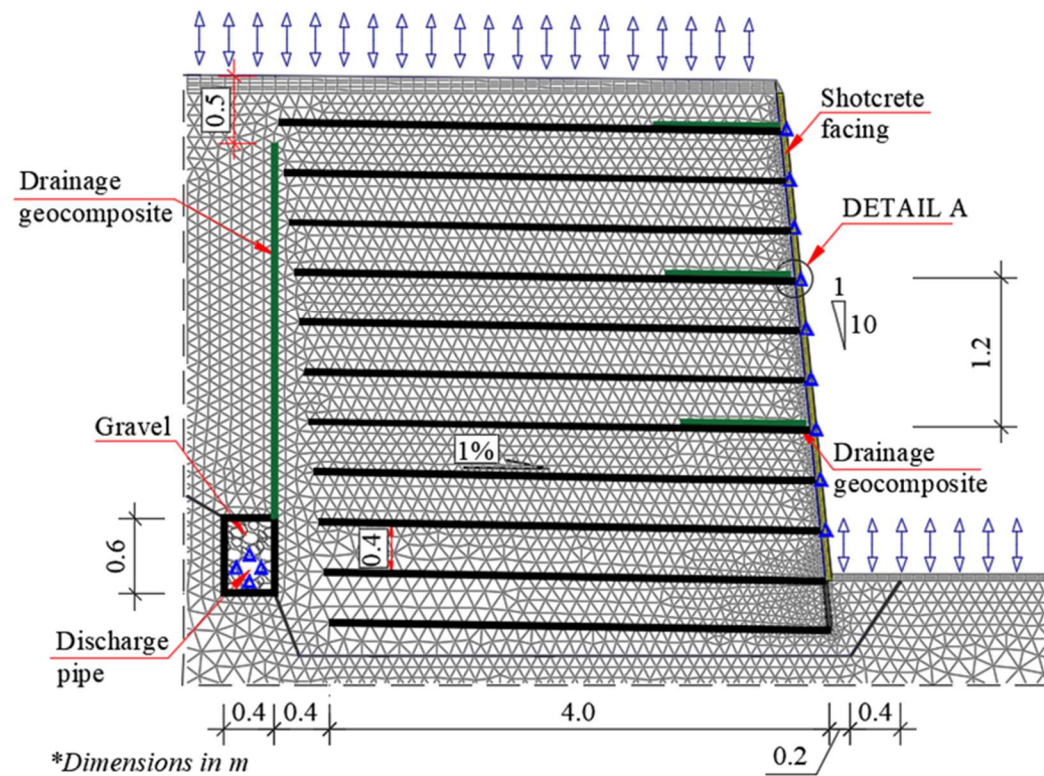
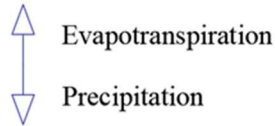


Figure 3.7 - Details of boundaries and properties for infiltration and evaporation simulations

In order to model the climate conditions and its effect on infiltration, the finite-element based software SEEPW (GEO-SLOPE, 2018a) was used to solve the

governing equation for transient flow in unsaturated conditions. The software solves the two-dimensional equation derived from Darcy's law by Richards (1931).

$$m_w \frac{\partial(u_a - u_w)}{\partial t} = \frac{\partial}{\partial y} \left[ \left( \frac{k_y}{\gamma_w} \right) \frac{\partial u_w}{\partial y} + k_y \frac{\partial y_e}{\partial y} \right] + \frac{\partial}{\partial x} \left[ \left( \frac{k_x}{\gamma_w} \right) \frac{\partial u_w}{\partial x} + k_x \frac{\partial y_e}{\partial x} \right] \quad (3.7)$$

where  $k_x$  and  $k_y$  are the hydraulic permeability in x and y direction, respectively;  $u_w$  is the pore water pressure;  $u_a$  is the pore air pressure;  $y_e$  is the elevation;  $\gamma_w$  is the unit weight of water; and  $m_w$  is the coefficient of water volume change (slope of the soil water retention curve).

### 3.5 Global stability analysis

In order to assess the stability of the field reinforced soil wall, limit equilibrium analyses were conducted considering the unsaturated shear strength of soil. Vanapalli *et al.* (1996) proposed the Equation 3.8 to model the soil unsaturated shear strength based on the soil water characteristic curve and the effective shear strength parameters of the soil. Equation 3.8 is an extension of the theory proposed by Fredlund, Morgenstern and Widger (1978) to compute soil unsaturated shear strength.

$$\tau = c' + (\sigma_n - u_a) \tan \phi' + (u_a - u_w) \left[ (\tan \phi') \left( \frac{\theta - \theta_r}{\theta_s - \theta_r} \right) \right] \quad (3.8)$$

where  $\tau$  is the shear strength,  $c'$  is the effective cohesion,  $\phi'$  is the effective friction angle,  $(\sigma_n - u_a)$  is the net normal stress on the failure plane,  $(u_a - u_w)$  is the matric suction;  $\theta_s$  and  $\theta_r$  were defined previously. The software SLOPE/W (GEO-SLOPE, 2018b) was used to assess global stability analysis using Equation 9 and the pore water pressure previously computed by SEEP/W (GEO-SLOPE, 2018b).

Morgenstern-Price method was used to calculate the factors of safety of the GRS wall under the effects of climatic changes. Only circular slip surface was assumed in the analyses. The entry and exit searching method was used to determine the critical slip surface, which consists of a variation of the grid-radius method. The entry and exit areas of possible slip surfaces were positioned as shown in Figure 3.8. The possible entry slip surfaces were assumed to initiate as the Culmann's critical slip surface and extend a maximum of 7 m from wall face. Exit area was assumed to start from the middle height of the GRS wall and extend 4 m beyond the wall toe. The number of

entries (above reinforced zone) and exits (between wall face and toe of GRS wall) was specified as 20 and 30, respectively. The spacing between each slip surface at the entry and exit areas resulted in 0.3 m and 0.2 m, respectively. In order to form a circle, the software connects a point along the entry area with a point along the exit area and, then a perpendicular line is created at the mid-point of it. The software SLOPE/W was set to divide the perpendicular line in 5 parts, creating 5 radius, and compute the factor of safety for each formed circle. The computational algorithm ensured that the entry and exit angle ( $\alpha$ ) of each slip surface did not exceeded 90 degrees and that no straight line (infinite radius) was used as possible slip surface. A total of 3,000 slip surfaces were checked for every day of analysis.

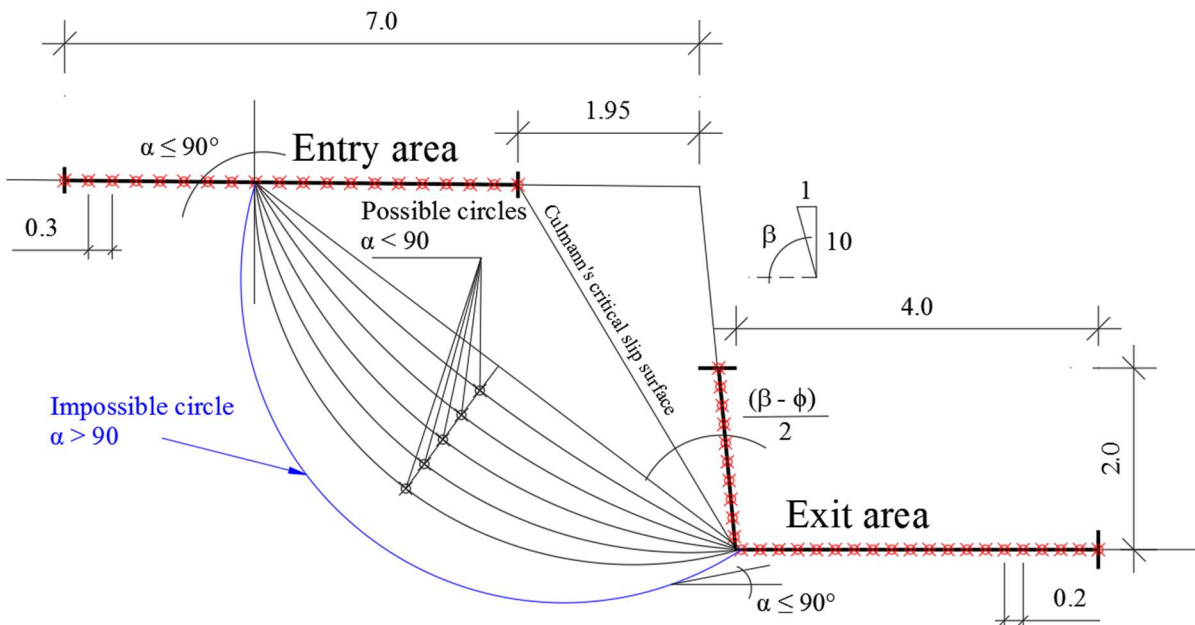


Figure 3.8 - Illustration of the entry and exit search method with the respective areas location used in this study

Nonwoven geotextile was assumed to contribute to global stability with a concentrated load in the limit equilibrium analyses. Experimental studies showed that the soil-reinforcement shear resistance increases due to soil unsaturated condition (FLEMING et al., 2006; HATAMI; ESMAILI, 2015). In this study, the shear resistance between soil and reinforcement was considered not to be affected by the soil unsaturated condition. SLOPE/W (GEO-SLOPE, 2018b) calculates the reinforcement pullout resistance using Equation 3.9. Then, the lowest value (pullout resistance;  $T_{max}$ ) of each reinforcement was used as a horizontal concentrated load in the equilibrium limit analysis.

$$\tau = c'_a + \sigma_v \tan \delta' \quad (3.9)$$

where  $\tau$  is the shear resistance;  $c'_a$  is the adhesion at soil-reinforcement interface, assumed as zero in this study;  $\sigma_v$  is the vertical stress;  $\delta'$  is the friction angle at soil-reinforcement interface calculated as a function of the soil friction angle as shown in Equation 3.10.

$$\tan \delta' = 0.7 \tan \varphi' \quad (3.10)$$

The nonwoven geotextile maximum allowable tensile force was calculated considering the reduction factor for installation, creep and damage as 1.10, 1.60 and 1.10, respectively. The combination of these factors resulted in a reduction factor of 1.94. Therefore, the allowable tensile force of the reinforcement was considered as 12.09 kN/m.

Stability analyses were conducted considering a surcharge of 20 kPa above the GRS wall.

## 3.6 Results and Discussion

### 3.6.1 Soil-atmosphere interaction

Figure 3.9 shows the water balance at ground surface over two years of rainfall and evaporation. Point A and B located at the top of the reinforced soil wall at 2 m and 7 m from wall face, respectively, were chosen to investigate actual evaporation, runoff and net infiltration. Net infiltration was computed as the difference between actual evaporation and runoff from the total applied rainfall. Figure 3.9a shows the cumulative actual evaporation that occurred at point A and B due to atmospheric demand for evaporation (i.e. potential evaporation, PE). Evaporation 2 m (A) and 7 m (B) from wall face were observed to be identical. The difference between potential and actual evaporation was significant, which indicate that approximately 50% of the potential evaporation turned into actual evaporation in both points A and B.

Figure 3.9b shows the comparison between the cumulative rainfall and the cumulative surface runoff. Surface runoff occurred when the rainfall rate was greater than soil infiltration capacity during torrential rainfall or in case of the soil was significantly dry to water infiltrate. Results show that cumulative surface runoff at point A (2 m from wall face) was similar to that occurred at point B (7 m from wall face). The

surface runoff was not significantly affected by the capillary effect when comparing results at A and B. Comparison of the cumulative rainfall and runoff show that 10% to 20% of the rainfall turns into runoff.

Figure 3.9c shows the cumulative net infiltration 2 m and 7 m from wall face compared to the cumulative rainfall. Similarly to the cumulative actual evaporation (Figure 3.9a), the water that infiltrates into the soil (i.e. net infiltration) is only a portion of the total rainfall. The results show that approximately 50% of the rainfall is converted into evaporation and runoff and the other 50% infiltrates. Comparison among Figure 3.9a, 3.9b with Figure 3.9c shows that the difference of cumulative rainfall and net infiltration occurred mainly because of actual evaporation. Additionally, the difference between net infiltration at point A and B was due to the surface runoff shown in Figure 3.9b. Although many studies showed that the capillary effect prevented water from infiltrating into reinforced soil structures with nonwoven geotextiles (IRYO; ROWE, 2005a; THUO et al., 2015; PORTELINHA; ZORNBERG, 2017; ALBINO et al., 2018; YANG et al., 2018), the comparison of net infiltration above (2 m from wall face) and outside (7 m from wall face) the reinforced zone, during a 2 years analyses, showed that capillary effect has no significant change on net infiltration.

Figure 3.9d compares the percentage of effective infiltration (i.e. ratio of cumulative net infiltration and rainfall) to effective evaporation (i.e. ratio of cumulative actual and potential evaporation, AE/PE) that occurred in point A and B. Results show that effective infiltration was initially zero and increased significantly over January of 2013. Also, both effective infiltration and evaporation varied significantly during the first 2 months of climate analysis. After 2 months, effective infiltration reduced and, after 2 years, this parameter was observed to be approximately 50% in both points A and B. The concept of effective infiltration has been used in hydrological studies (BONACCI, 2001; JEMCOV; PETRIC, 2009; ROSSI; DONNINI, 2018). Rossi and Donnini (2018) compiled effective infiltration data from some published studies. The compilation revealed the effective infiltration value vary from 15% to 88% depending on soil present in each catchment. These data are in accordance to the effective infiltration determined in the current study.

Figure 3.9d also shows that actual evaporation (AE) correspond to 40% of the potential evaporation (PE) in view of the initial water content (optimum water content) of backfill soil, which provided some water to evaporate. The value of 40% found in

this study is in agreement to findings of Baier and Robertson (1966). The authors showed that the ratio AE/PE two weeks after harvesting of a wheat crop (i.e. soil was exposed to atmosphere demand for evaporation) dropped from 90% to 50%. Also, Wilson, Fredlund and Barbour (1997) showed experimentally that the ratio AE/PE may start at 100% if soil is fully saturated and may reduce to 0 depending on the soil matric suction.

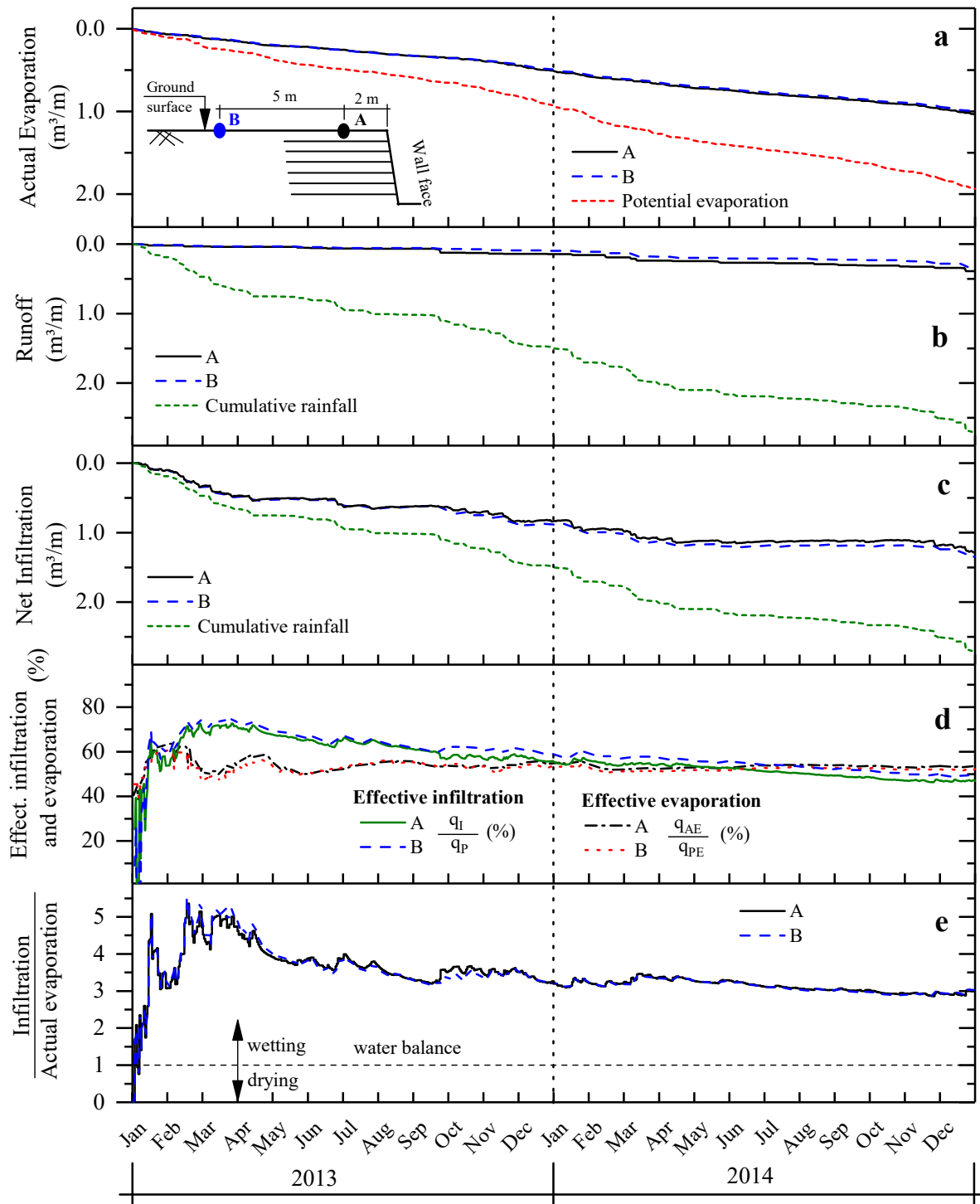


Figure 3.9 - Water balance over two years of climate analysis

Figure 3.9e shows the ratio of infiltration (i.e. difference of cumulative rainfall and cumulative runoff) and actual evaporation. This ratio provides a clear understanding of the water balance at ground surface. A ratio higher than 1 indicates more water infiltrating into the soil than evaporating. Ratio of infiltration and actual evaporation equal to 1 means that water balance has been achieved. Results show that water started to infiltrate in a much higher rate than it was evaporating from January to May of 2013. After that, the ratio of infiltration and actual evaporation started to reduce slowly tending to 1. However, the numerical analysis indicates that water balance was not achieved during two years of operation since the ratio of infiltration and actual evaporation did not reach the value of 1. Also, the cumulative volume of water infiltrating into the soil was observed three times lower than the evaporation volume after 2 years of operation.

### 3.6.2 Climate effects on pore water pressure and global factor of safety

Climate effects on stability of the GRS was evaluated based on nine points of analyses located inside and outside of the reinforced zone as illustrated in Figure 3.6. Figure 3.10 shows the changes in soil suction, as well as, the changes in factor of safety (FoS) under climatic changes between 2013 and 2014. Figure 3.10a shows the daily and accumulative precipitation applied during the period of analysis, as well as, the cumulative net infiltration. The seasons of 2013 and 2014 were presented previously in Figure 3.2 where spring and summer were clearly defined as the wetting seasons. Figure 3.10b shows the changes in soil suction along section A (1 m from wall face). Results show that after two months of climate analysis the soil suction at A1, A2 and A3 were observed to be below 20 kPa indicating that the soil did not return to initial value of suction (45kPa) during the period of study (i.e. 2 years) even considering evaporation. Decreases in suction along section A were observed to be consistent to occurred precipitation events. In July and the period between October and December of 2013, the soil suction decreases were preceded by frequent precipitation events. On the other hand, from May to December of 2014 no significant decrease in suction was observed indicating that a minimum period of infiltration is necessary to cause the breakthrough of water at geotextile interfaces and, consequently, significant changes in suction inside the reinforced zone. Figure 3.10c showed a similar trend of that observed in Figure 3.10b, where suction values were

observed to decrease due to previous precipitation events as observed along section A and observed to reach values lower than 25kPa. Also, no significant decreases in suction were observed between May and December of 2014 due to short period of successive days of precipitation to cause breakthrough of water and affect suction inside the reinforced zone. Figure 3.10d shows the suction changes outside the reinforced zone. Results show that, differently of points A1, (Figure 3.10b) and B1 (Figure 3.10c), the point C1 had a more significant change of suction under the effect of climatic changes for 2 years. Additionally, from May to December of 2014, a significant variation in suction was observed at C1 while no significant variation occurred at A1 and B1. These variations are due to the natural water balance process that occurs near ground surface. The same process was not observed at A1 and B1 in view of the presence of nonwoven geotextiles and the development of capillary barrier, which prevented water of infiltrating during low intensity precipitations. Suction decreases showed good agreement with precipitation events shown in Figure 3.10a. Figure 3.10e shows the variation of the global factor of safety of the reinforced soil structure over the two years of climate analysis. Additionally, Figure 3.10e shows the minimum factor of safety considering the soil totally saturated. Comparing Figure 3.10a and 3.9e the successive days of rainfalls reduced the factor of safety to values close to the saturated value. From January to April of 2013 consecutive days of precipitation caused a significant reduction on factor of safety from 3 to approximately 1.8. Similar patterns of consecutive days of precipitation and drop in factor of safety were also observed during the climate analysis. From May to December of 2014 when successive days of precipitation were less pronounced, and water infiltrating was reduced into section A and B, as showed in Figure 3.10b and 3.9c, the factor of safety showed higher values. These results indicate that water may infiltrate into the reinforced soil wall in two case scenarios: (1) torrential rainfall; (2) consecutive days of precipitation. Additionally, these results indicate that for the rainfall regime of the São Paulo city, Brazil, the reinforced soil walls should be designed considering that soil would become saturated and the factor of safety could drop to its minimum value. For different regions with different rainfall regimes, the wall stability should be analyzed following the soil-atmosphere procedure presented in this chapter.

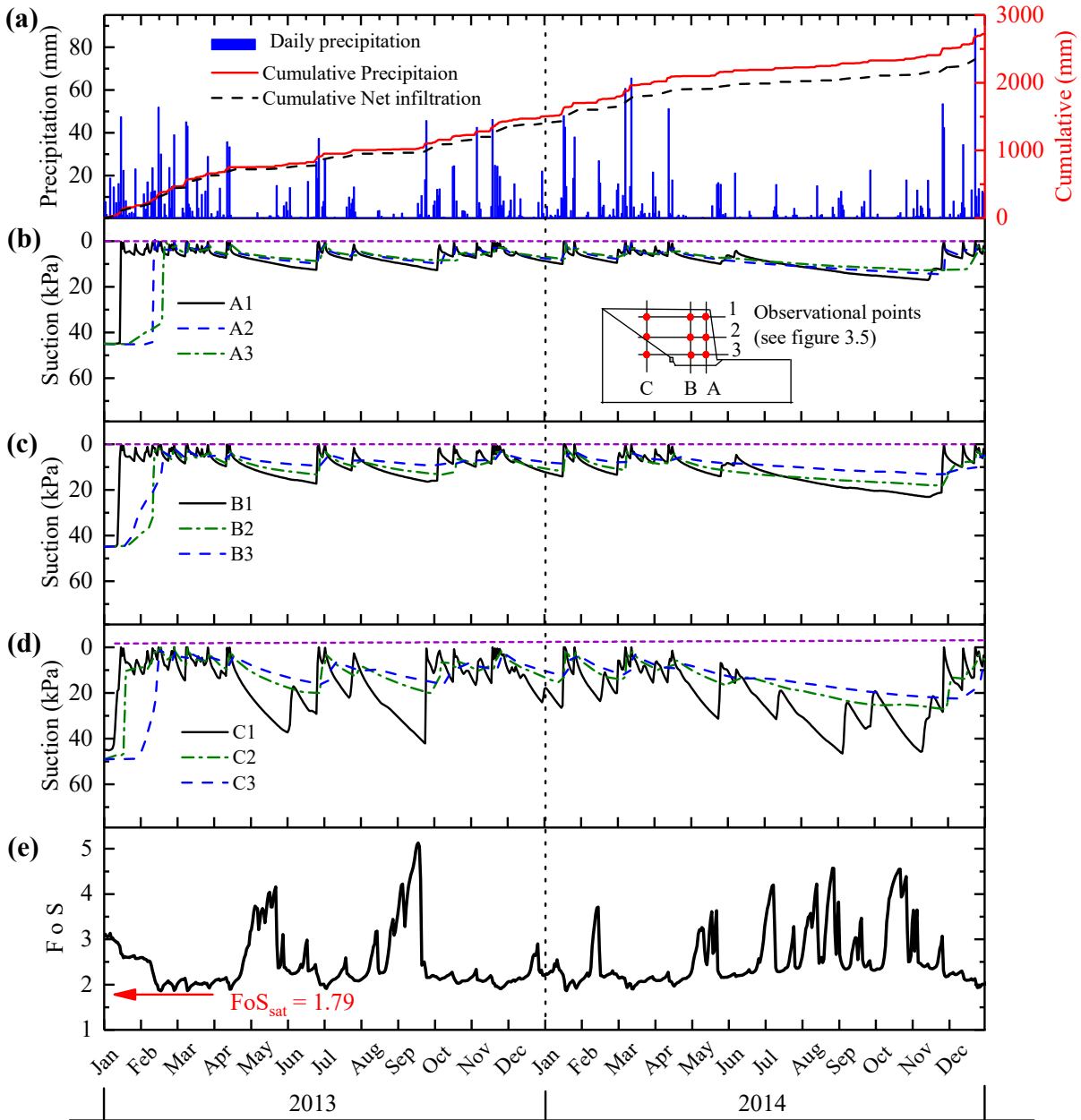


Figure 3.10 - Precipitation change in pore water pressure and global factor of safety

Figure 3.11 shows the impact of nonwoven geotextile on water advancement. Figure 3.11a shows the daily precipitation for comparison of changes in PWP and saturation during the analyses. Figure 3.11b shows the change in saturation above and below the first reinforcement layer of nonwoven geotextiles (NWG). Above the nonwoven geotextile results show that soil was subjected to changes on degree of saturation due to precipitation and evaporation. Increases on degree of saturation were observed to follow the precipitation rate shown in Figure 3.11a. On the other hand, below NWG where soil became saturated between January and February of 2013, the evaporation was not able to remove water and reduce the degree of saturation of the backfill soil. The result indicates that the capillary barrier affects evaporation of water infiltrated in the reinforced zone. During 2014, the saturation above NWG was observed to remain below the degree of saturation of compacted soil corroborating to the fact that changes in degree of saturation of soil or PWP requires consecutive raining days.

Figure 3.11c compares the variation of suction above the upper reinforced layer at 2 m and 7 m from wall face. Differently from Figure 3.10 where points A1, B2 and C1 were located 600 mm from ground surface, these results were obtained for the middle height of the upper reinforced layer (300 mm from ground surface). Comparing Figure 3.10b (A1) and 3.10d (C1) to Figure 3.11c and 3.11d, respectively, it is clear that as closer to soil surface, higher is the impact of the climatic changes on soil suction. Also, suction values at 2 m and 7 m from wall face indicate that the nonwoven geotextile prevent water from infiltrating due to capillary barrier effect and cause suction increases. This excessive increase in suction may lead soil to become too dry, develop cracks and consequently increase hydraulic permeability. The change in permeability due to crack formation because of drying was not considered in this study. Additionally, raining and non-raining days showed to lead to decreases and increases in suction, respectively. More concentrated increases of suction were observed from May to December of 2014 because of the less consecutive days of precipitation.

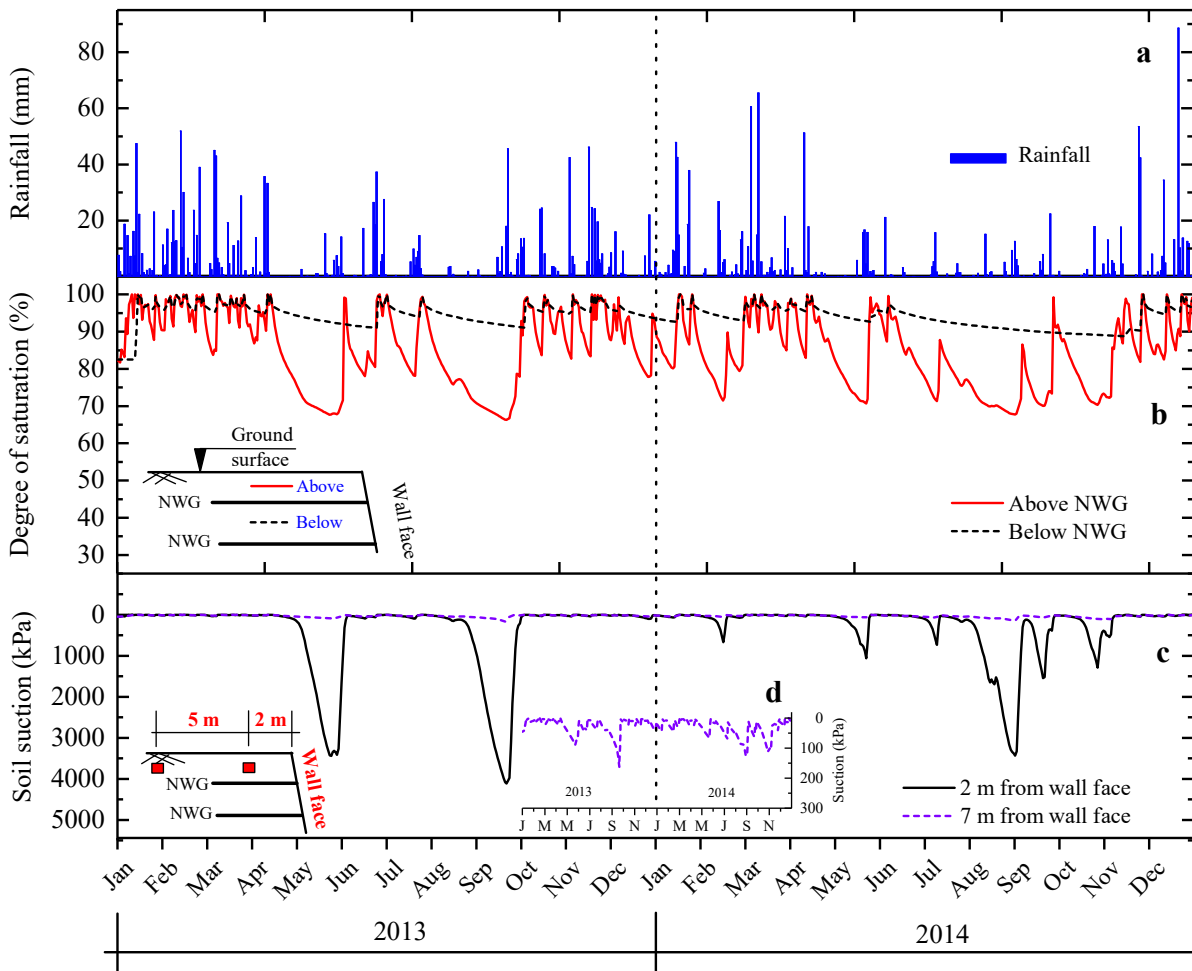


Figure 3.11 - Nonwoven geotextile (NWG) influence in water advancement.

Figure 3.12a shows the wetting advancement in section C, 7 m from wall face (i.e. out of the reinforced zone, see Figure 3.6). Results show that 9 days after the climatic analyses water advanced 1.0 m into the soil. Five days later (day 14) water advanced more 0.8 m reaching the elevation 2.2 m. These results indicate that water advancement during the first 9 days was less intense than from day 9 to day 14. After 30 days results indicate that water advanced into the soil 7 m from wall face reducing soil suction significantly throughout the depth. From day 30 to day 44, results show that water advancement was reduced. Additionally, the water advanced a distance equal in value to the height of the GRS wall reducing the soil suction to values below 25 kPa. After 50 days of climatic analyses soil suction was observed below 10 kPa and subsequent variations in suction, on day 58 and 89, were observed to occur mainly in elevations higher than 3.5 m. These variations near ground surface (i.e.  $Y = 4.0$  m) occurred because of the soil-atmosphere interaction. The results of Figure 3.12a (7 m from wall face and out of the reinforced zone) compared to the results of Figure 3.12b

(3 m from wall face and inside the reinforced zone) show that water advancement into the reinforced zone was delayed. This occurred because of the capillary break at soil-geotextile interface that delayed the water advancement into the reinforced zone during precipitation events.

Figure 3.12b shows the wetting of the GRS (i.e. geosynthetic reinforced soil) wall through the changes in suction during the first 89 days of 2013. The suction profiles shown in Figure 3.12b represent the section B showed in Figure 3.6. Results indicate that the advancement of the wetting front causes the reduction of the soil suction and the factor of safety. After 9 days of climatic analyses the factor of safety was 2.97 and the water front was about 0.5 m from the top of the wall. After 14 days the wetting front was observed to advance 0.8 m in relation to day 9 and the factor of safety was observed to drop a little. Additionally, the suction was observed to be 0 kPa above the elevation 3.4 m. Comparing the water advancement from day 9 to day 44, it can be observed that the water advancement was not constant over time because of precipitation, evaporation and capillary barrier effects. After 50 days of climate analyses the water front was observed to reach the bottom of the reinforced soil wall and suction across the GRS wall elevation was observed below 20 kPa. After 58 days of climate analyses the lowest factor of safety of 1.87 was observed. This low factor of safety occurred because suction across the elevation of the wall was less than 5 kPa. This low factor of safety was close to that for a saturated soil condition showed in Figure 3.10. After 89 days of climatic changes the suction profile was observed below 15 kPa and factor of safety was slightly above 2.00. Figure 3.12b also shows that less than 60 days were necessary to the nonwoven geotextile reinforced soil wall reduce the initial suction of 45 kPa to values close to 0 kPa. The suction values shown in Figure 3.12b compared to the soil water retention curve showed in Figure 3.4 indicate that the soil saturated in less than 2 months of climatic analyses.

Figure 3.12a and 3.12b showed that water advancement into the soil outside (section C) and inside (section B) of the reinforced zone, respectively, was not constant. These results can be better explained with Figure 3.12c. Figure 3.12c show the net infiltration into the soil in both sections B and C during the first 89 days of climatic analyses. The faster advancement of water from day 9 to day 14 can be clearly explained by the increase in net infiltration in both sections B and C. Additionally, the delayed advancement of water into the soil in both section B and C from day 14 to day

39 is also shown through the net infiltration that increased slightly through time. From day 39 to day 58 the net infiltration was observed to increase significantly in both sections and soil suction was observed to reduce accordingly. After day 58, the soil in both section B and C experienced first wetting and subsequent increase in net infiltration was observed to cause small soil suction variations. Also, Figure 3.12c shows that the increase in net infiltration led to a reduction in the wall factor of safety over time. However, the same reduction in the factor of safety was not observed on day 89. That occurred because of the increase in soil suction above 3.5 m (showed in both section B and C) which led to an increase in soil shear strength and consequently increased the factor of safety.

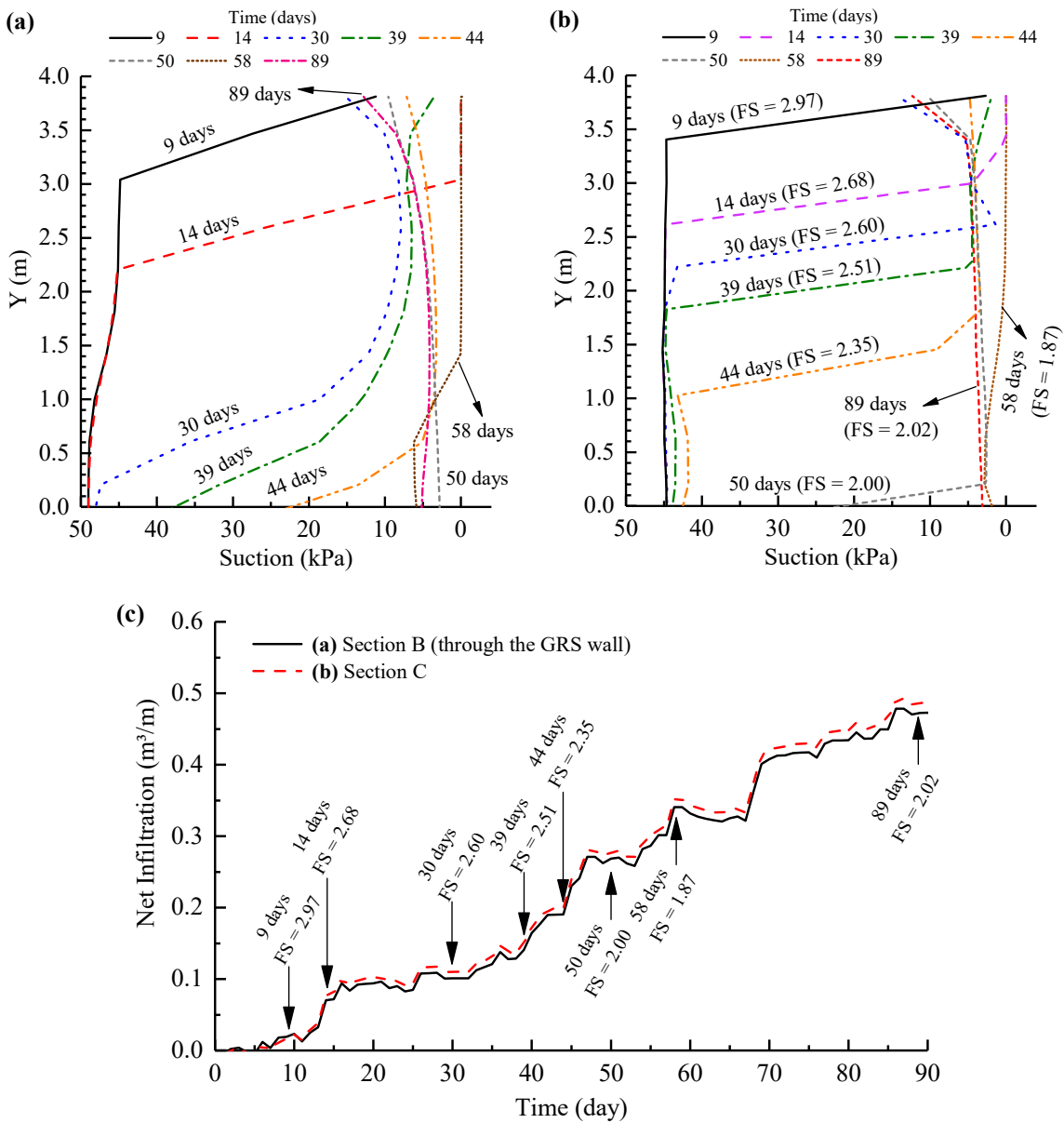


Figure 3.12 - (a) Suction profiles 7 m from wall face (section C); (b) Suction profiles 3 m from wall face (section B); (c) Changes in net infiltration over 89 days of climatic analyses.

Figure 3.13a illustrates the pore water pressure distribution in the model after 39 days of climatic analyses. The result shows that water front advanced faster outside the reinforced zone when compared to inside the reinforced zone. Inside the reinforced zone water was observed to advance approximately 2 meters ( $Y = 2$  m), while outside the reinforced zone the water was observed to advance approximately 3 meters ( $Y = 1$  m). This occurred due to the capillary effect caused by the nonwoven geotextile preventing water from infiltrating freely. Figure 3.13b shows the results from stability analyses resulting in a critical factor of safety of 2.51. Additionally, Figure 3.13b showed in red the safety map zone corresponding to an increment of 0.1 in the factor of safety. In other words, inside this zone are present the factors of safety between 2.51 and 2.61.

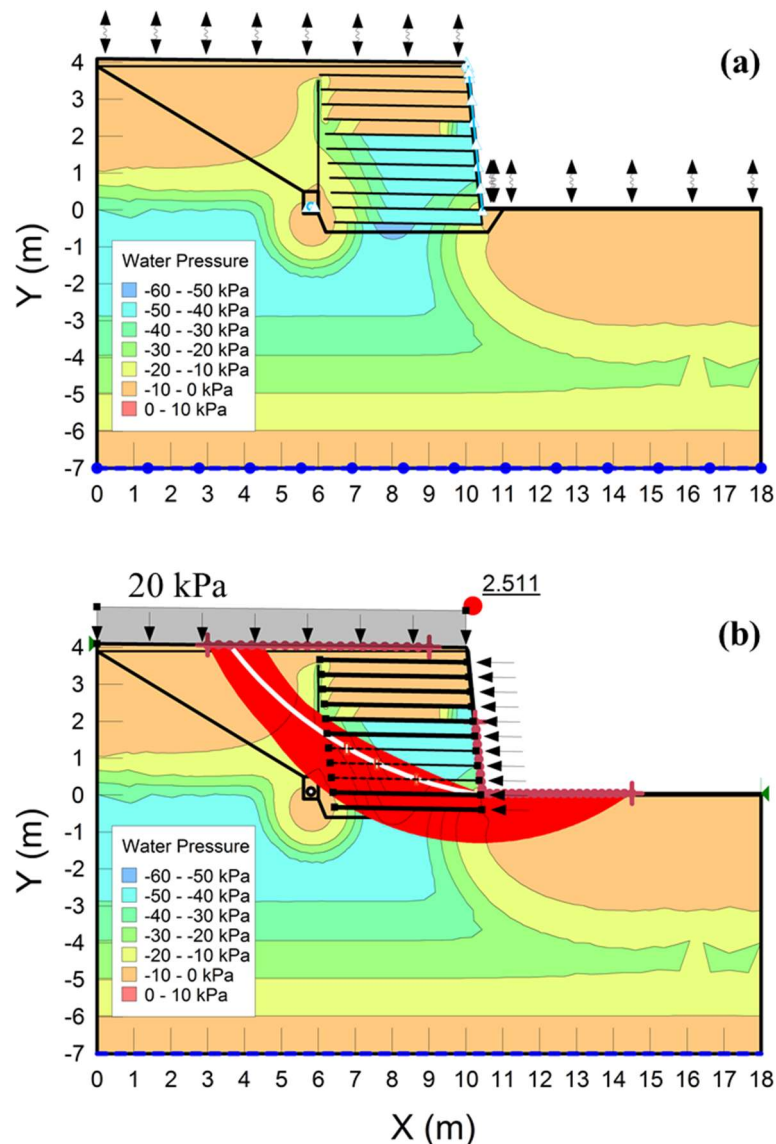


Figure 3.13 - (a) Pore water pressure distribution after 39 days of climatic analyses;  
(b) The factor of safety after 39 days of climatic analyses



Figure 3.15 shows the suction profiles along the soil elevation inside and outside of the GRS wall in different days of the 2 years of climatic analyses. Figure 3.15 is a complement of Figure 3.12 showing some suction profiles after water completely advance throughout the GRS wall for the first time.

Figure 3.15a shows suction profiles outside of the reinforced zone (section C). Results show that after 260 days of climatic analyses soil suction values were as high as 200 kPa. Soil suction near ground surface after 148, 260 and 603 days of climatic analysis were observed above the initial condition (45 kPa) indicating that evaporation increased soil suction. On the other hand, soil suction near ground surface after 184; 382 and 432 days of climatic analysis were below 10 kPa. Figure 3.15b shows the decrease in soil suction below elevation 3.4 m that were not clearly shown in Figure 3.15a. Suction values below elevation 3.4 m were observed less than initial condition (45kPa) after day 148, 260 and 603, while after day 184, 382 and 432 the suction values below the same elevation were less than 15 kPa. Additionally, near elevation 0.0 m the suction values were observed between 10 kPa and 20 kPa in all days showed in Figure 3.15a.

Figure 3.15c shows that above the first reinforcement layer (i.e. elevation above 3.4 m) soil suction varies considerable because of the climatic variations. Suction values above the first reinforcement layer were observed as high as 4000 kPa (also shown in Figure 3.11c). Figure 3.15d shows that below the first reinforcement layer soil suction varied below 15 kPa and did not returned to its initial condition of 45 kPa. However, the reduced value of soil suction below the first reinforcement layer was not observed to reduce the factor of safety after 148, 260 and 603 days of climatic analyses. The low values of soil suction below the first reinforcement layer contrasting to higher values of soil suction above the first reinforcement layer indicate that the capillary effect prevented the soil, surrounded by the nonwoven geotextile, of drying during non-rainy days. Figure 3.15d also shows that when a lower factor of safety was computed the suction profile along the elevation of the wall was below 10 kPa. As mentioned before, Figure 3.4 showed that for values below 10 kPa the soil is practically saturated. This explains the reason for the reduction in the factor of safety observed on days 184, 382 and 184.

Comparison of suction profiles 7 m (Figure 3.15a and b) and 3 m (Figure 3.15c and d) from wall face indicates that the nonwoven geotextile continued preventing water from evaporating (as also observed in Figure 3.12) even after first wetting of the GRS wall. Additionally, the high values of suction above elevation 3.4 m showed good agreement with higher values of factor of safety indicating that the surface soil suction governed the factor of safety in the stability analyses conducted in this study.

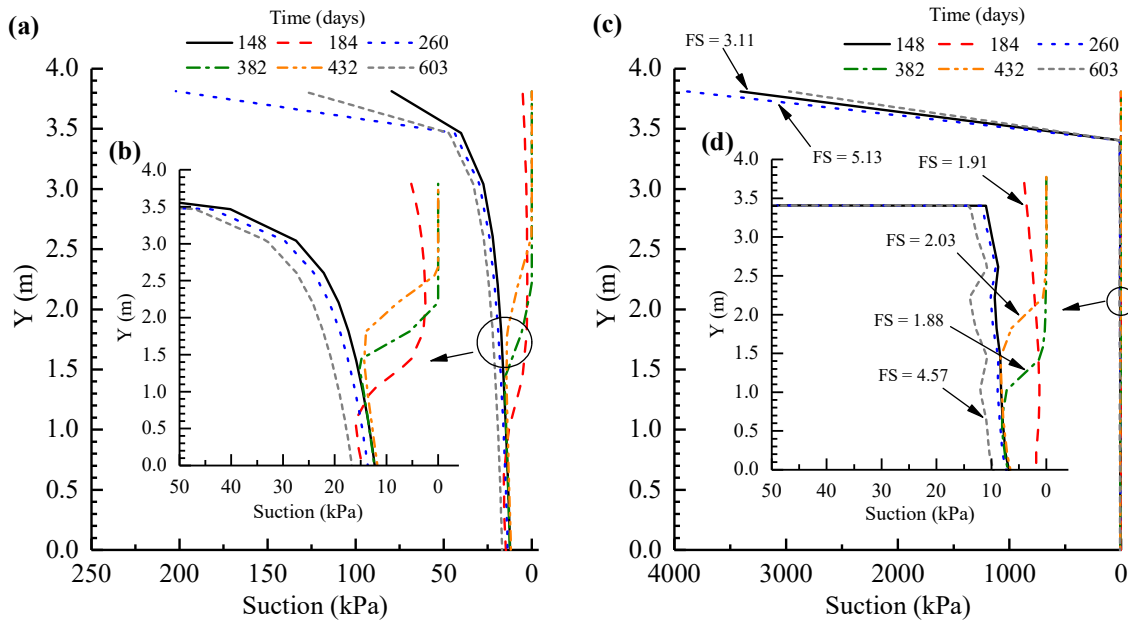


Figure 3.15 - Suction profile for different days. (a) 7 m from wall face (section C, see Figure 3.6); (b) 3 m from wall face (section B, see Figure 3.6)

Figure 3.16 shows the relationship between the cumulative precipitation during consecutive days of precipitation and the factor of safety. The results show that, an increase of cumulative precipitation generates a decrease in the factor of safety. Also, results show that the number of consecutive days of precipitation is not directly related to the factor of safety. For example, cumulative precipitation for 7 consecutive days were observed below some values for 5 days of consecutive precipitation. Figure 3.16 also shows that one event of five days of consecutive precipitation presented higher cumulative precipitation and factor of safety than others precipitation events with similar cumulative values. This difference was observed at day 16 of the climate analysis during the first wetting of the GRS wall. At this moment of the climate analysis, the water was observed to advance into the wall approximately 1.5 m (see Figure 3.12b). Results show that for five or more days of consecutive precipitation, the factors of safety were observed below the initial factor of safety of 3.1. Figure 3.16 also shows the path for consecutive days of precipitation during the first wetting of the GRS wall.

The lowest factor of safety and the higher cumulative precipitation value was observed after 11 days of consecutive precipitation (day 48 of the climate analysis). This low factor of safety and high cumulative precipitation value was observed to occur during the first wetting of the GRS wall.

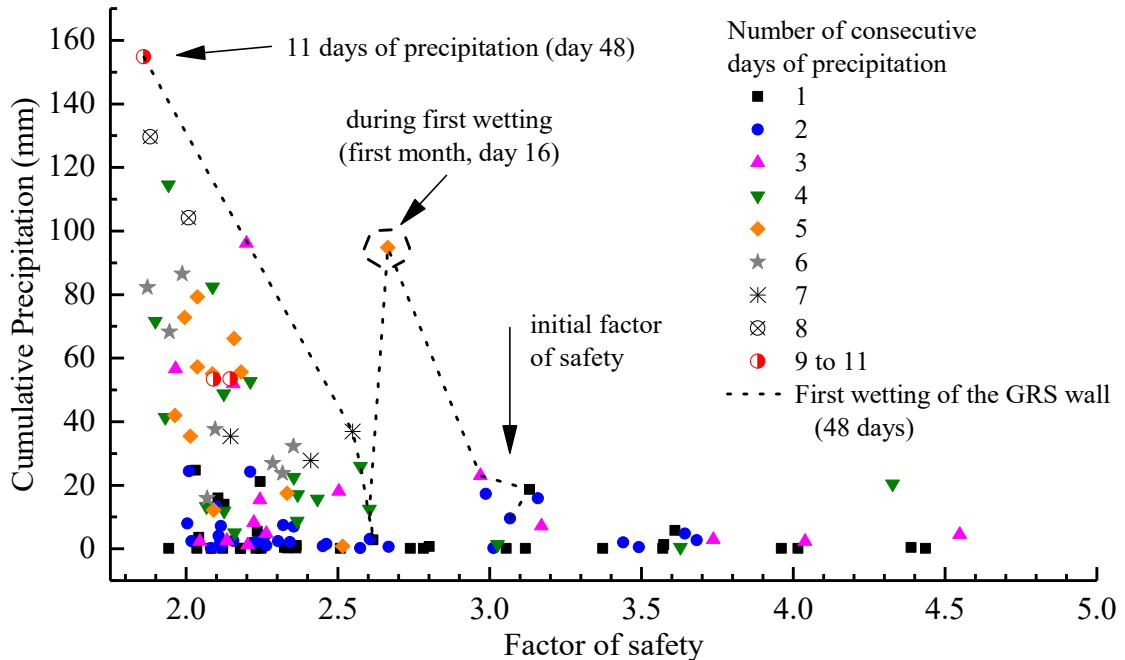


Figure 3.16 - Relationship of cumulative precipitation during consecutive rainy days with the factor of safety

### 3.7 Conclusions

This chapter presents a simple numerical methodology to simulate climatic changes involving infiltration and evaporation on suction of a geosynthetic-reinforced soil wall. In order to assess climate effects on stability structure, a reinforced soil wall was modelled using nonwoven geotextile reinforcements and submitted to daily precipitation and evaporation over a period of two years considering the climatic changes in São Paulo city, Brazil. The numerical simulations conducted in this study yielded the following conclusions:

- Simulations showed that approximately 50% of the potential evaporation becomes actual evaporation while net infiltration correspond to 50% of the total precipitation. Additionally, the results revealed that 10% to 20% of the total precipitation turned into surface runoff.
- The capillary effect caused by nonwoven geotextile as reinforcements of clayey sand used in this study did not generated significant runoff above the reinforced

soil wall and reduction of the cumulative net infiltration when compared to the unreinforced zone.

- After 2 years of climate analysis, the numerical analyses showed that the water balance was not achieved and the cumulative volume of water infiltrating into the soil was three times lower than the evaporation volume.
- Decreases of soil suction at monitored points inside of the nonwoven geotextile reinforced soil wall showed to be influenced by previous successive rainfall events or torrential rainfall events.
- Changes in soil suction inside and outside of the geosynthetic reinforced wall showed different patterns during the climatic analyses because of the capillary break at soil-geotextile interface. Water was observed to advance faster outside of the reinforced zone than inside of the reinforced zone because of the capillary barrier effect.
- Decreases in global factor of safety were observed after consecutive days of precipitation. Additionally, the results suggest that for the rainfall regime of São Paulo city, Brazil, GRS walls should be designed considering that soil could become saturated and the factor of safety could drop to its minimum value.
- Simulations showed that suction changes at the upper layer of the reinforced soil wall was more significant than outside of the reinforced zone. The capillary break at soil-geotextile interface occurring over the upper reinforced layer acted as a barrier restricting evaporation. Interestingly, only the soil above the first reinforced layer lost water due to evaporation. Therefore, higher suction values were observed above the top reinforcement layer and consequent increases in the factors of safety were observed.
- Geocomposites installed at wall face were observed to improve lateral drainage and prevent water from accumulate near wall face.
- Numerical simulation showed that, after first wetting of the GRS wall subjected to precipitation and evaporation processes, the initial value of soil suction did not return to the initial value of 45 kPa, even after evaporating events. This occurred because of the nonwoven geotextile capillary effect that prevented water from evaporating. Thus, suction profiles shown (Figure 3.15c and 3.15d)

for different days showed that soil suction was maintained below 15 kPa inside the reinforced zone.

- Changes in global factor of safety showed some correlation to cumulative precipitation during successive days of rainfall. Also, an increase on consecutive days of precipitation did not indicate a reduction in the factor of safety.



#### 4. GENERAL REMARKS

This study was conducted to better understand the behavior of a geosynthetic soil wall reinforced, mainly those constructed with nonwoven geotextiles, subjected to climatic changes using numerical simulations.

Firstly, the infiltration process into a full-scale laboratory reinforced soil wall was numerically evaluated using the software SEEP/W (GEO-SLOPE, 2018a). The infiltration modeling was firstly conducted including the capillary effect based on the experimental and monitored model of reinforced soil wall reported by Portelinha and Zornberg (2017). Afterwards, water advancement was evaluated in regions that were not monitored during the laboratory experiment. Results showed that water may change direction towards the wall face because of the reinforcement anchorage length. Water breakthrough was found to occur near wall face and at the back of the wall depending on the position of the drainage geocomposites. Additionally, the numerical calibration conducted using two measured variables (pore water pressure and volumetric water content) indicated that non-uniformly breakthrough of water occurred along the geotextile plane. Therefore, capillary barrier efficiency may be carefully evaluated through numerical analysis for application such as landfill.

Secondly, the curves that better represented the water infiltration process in the laboratory experiment were used to simulate the impact of real climatic changes on the stability of a hypothetical reinforced soil wall. The study was conducted using 2 years of real climatic data from the state of São Paulo, Brazil. The climatic data was chosen based on the historical precipitation average from 1933 to 2017. Results revealed that changes in soil suction were related to cumulative precipitation occurred during previous days of successive precipitation. The reinforced soil wall was observed to become fully wet after 90 days of analyses. Evaporation events were observed to increase the global factor of safety. Suction inside the reinforced zone was observed to vary below 20 kPa after first wetting of the reinforced zone and never return to initial condition (45 kPa). Global stability analyses considering the soil unsaturated shear strength revealed that the structure experienced factor of safety close to that of a fully saturated soil (e.g. cohesive contribution to shear equal to zero). Therefore, results indicated a GRS wall subjected to the climate effects of the São Paulo city, Brazil, should be designed considering that the soil may become fully saturated.



## REFERENCES

- ALBINO, U. R.; PORTELINHA, F. H. M.; ZORNBERG, J. .; FUTAI, M. M. **Numerical study of infiltration in a large-scale laboratory geotextile-reinforced soil wall.** 2018.
- ANDERSON, J. An ecological engineering approach for keeping water from reaching interred wastes in arid or semiarid regions. International Containment Technology Conference. **Anais...** . p.243–251, 1997.
- ASTM D2487. Standard Practice for Classification of Soils for Engineering Purposes (Unified Soil Classification System). **ASTM International**, v. D2487-11, p. 1–12, 2011.
- ASTM D5298. Standard Test Method for Measurement of Soil Potential (Suction) Using Filter Paper. **ASTM International**, p. 6, 2012.
- ASTM D6836. Standard Test Methods for Determination of the Soil Water Characteristic Curve for Desorption Using Hanging Column, Pressure Extractor, Chilled Mirror Hygrometer, or Centrifuge. **ASTM International**, p. 20, 2012.
- BAHADOR, M.; EVANS, T. M.; GABR, M. A. Numerical studies on the effect of temperature on the unsaturated hydraulic response of geotextiles. **Computers and Geotechnics**, v. 59, p. 161–170, 2014.
- BAIER, W.; ROBERTSON, W. A new versatile soil moisture. **Canadian Journal of Plant Science**, v. 46, p. 299–315, 1966.
- BALAKRISHNAN, S.; VISWANADHAM, B. V. S. Performance evaluation of geogrid reinforced soil walls with marginal backfills through centrifuge model tests. **Geotextiles and Geomembranes**, v. 44, n. 1, p. 95–108, 2016.
- BATHURST, R. J.; HO, A. F.; SIEMENS, G. A column apparatus for investigation of 1-D unsaturated-saturated response of sand-geotextile systems. **Geotechnical Testing Journal**, v. 30, n. 6, p. 433–441, 2007.
- BENJAMIM, C. V. S.; BUENO, B. S.; ZORNBERG, J. G. Field monitoring evaluation of geotextile-reinforced soil-retaining walls. **Geosynthetics International**, v. 14, n. 2, p. 100–118, 2007.
- BERG, R. R.; CHRISTOPHER, B. R.; SAMTANI, N. C. **Design and construction of mechanically stabilized earth walls and reinforced soil slopes–Volume I.** 2009.
- BHATTACHERJEE, D.; VISWANADHAM, B. V. S. Numerical studies on the performance of hybrid-geosynthetic-reinforced soil slopes subjected to rainfall. **Geosynthetics International**, v. 22, n. 6, p. 411–427, 2015.
- BONACCI, O. Monthly and annual effective infiltration coefficients in Dinaric karst: example of the Gradole karst spring catchment. **Hydrological Sciences Journal**, v.

46, n. 2, p. 287–299, 2001.

BUENO, B. S.; BENJAMIM, C. V. S.; ZORNBERG, J. G. Field performance of a full-scale retaining wall reinforced with nonwoven geotextiles. **Geotechnical Special Publication**, , n. 130–142, 2005.

CHINKULKIJNIWAT, A.; HORPIBULSUK, S.; BUI VAN, D.; et al. Influential factors affecting drainage design considerations for mechanical stabilised earth walls using geocomposites. **Geosynthetics International**, v. 24, n. 3, p. 1–18, 2017.

CUOMO, S.; MOSCARIELLO, M.; FORESTA, V. Wetting tests of partially saturated soils under simple shear conditions. **Géotechnique Letters**, v. 7, n. 2, p. 1–7, 2017.

DURNER, W. Hydraulic Conductivity Estimation for Soils with Heterogeneous pore Structure. **Water Resources Research**, v. 30, n. 2, p. 211;223, 1994.

EL-NESR, M. N.; ALAZBA, A. A.; ŠIMŮNEK, J. HYDRUS simulations of the effects of dual-drip subsurface irrigation and a physical barrier on water movement and solute transport in soils. **Irrigation Science**, v. 32, n. 2, p. 111–125, 2014.

ERHLICH, M.; VIDAL, D.; CARVALHO, P. A. Performance of two geotextile reinforced soil slopes. Recent Development in soil and Pavement Mechanics. **Anais...** . p.415–420, 1997.

ESMAILI, D.; HATAMI, K.; MILLER, G. A. Influence of matric suction on geotextile reinforcement-marginal soil interface strength. **Geotextiles and Geomembranes**, v. 42, n. 2, p. 139–153, 2014.

FHWA. **Design and construction of mechanically stabilized earth walls and reinforced soil slopes**. 2009.

FLEMING, I. R.; SHARMA, J. S.; JOGI, M. B. Shear strength of geomembrane–soil interface under unsaturated conditions. **Geotextiles and Geomembranes**, v. 24, p. 274–284, 2006.

FREDLUND, D. G.; MORGENSTERN, N. R.; WIDGER, R. A. The shear strength of unsaturated soils. **Canadian Geotechnical Revue canadienne**, v. 321, p. 313–321, 1978.

GARCIA, E. F.; GALLAGE, C. P. K.; UCHIMURA, T. Function of permeable geosynthetics in unsaturated embankments subjected to rainfall infiltration. **Geosynthetics International**, v. 14, n. 2, p. 89–99, 2007.

GASMO, J. M.; RAHARDJO, H.; LEONG, E. C. Infiltration effects on stability of a residual soil slope. **Computers and Geotechnics**, v. 26, n. 2, p. 145–165, 2000.

GENUCHTEN, M. T. VAN. A Closed-form Equation for Predicting the Hydraulic Conductivity of Unsaturated Soils. **Soil Science Society of America Journal**, v. 44, n. 5, p. 892, 1980.

GEO-SLOPE. Seepage modeling with SEEP/W 2018. Calgary, Canada: GEO-SLOPE International Ltd. , 2018a.

GEO-SLOPE. Stability modeling with SLOPE/W 2018. Calgary, Canada: GEO-SLOPE International Ltd. , 2018b.

GIDIGASU, M. D. **Laterite Soil Engineering Pedogenesis and Engineering Principles**. Amsterdam: Elsevier, 1976.

GRIFFITHS, D. V.; LU, N. Unsaturated slope stability analysis with steady infiltration or evaporation using elasto-plastic finite elements. **International Journal for Numerical and Analytical Methods in Geomechanics**, v. 29, n. 3, p. 249–267, 2005.

HATAMI, K.; ESMAILI, D. Unsaturated soil – woven geotextile interface strength properties from small-scale pullout and interface tests. **Geosynthetics International**, v. 22, n. 2, p. 161–172, 2015.

HENRY, K. S.; HOLTZ, R. D. Geocomposite capillary barriers to reduce frost heave in soils. **Canadian Geotechnical Journal**, v. 38, n. 4, p. 678–694, 2001.

HOLMÉN, J. G.; STIGSSON, M. **Modelling of future hydrogeological conditions at SFR**. Stockholm, Sweden, 2001.

IRYO, T.; ROWE, R. K. On the hydraulic behavior of unsaturated nonwoven geotextiles. **Geotextiles and Geomembranes**, v. 21, n. 6, p. 381–404, 2003.

IRYO, T.; ROWE, R. K. Numerical study of infiltration into a soil–geotextile column. **Geosynthetics International**, v. 11, n. 5, p. 377–389, 2004.

IRYO, T.; ROWE, R. K. Infiltration into an embankment reinforced by nonwoven geotextiles. **Canadian Geotechnical Journal**, v. 42, n. 4, p. 1145–1159, 2005a.

IRYO, T.; ROWE, R. K. Hydraulic behaviour of soil – geocomposite layers in slopes. **Geosynthetics International**, v. 12, n. 3, p. 145–155, 2005b.

ITYEL, E.; LAZAROVITCH, N.; SILBERBUSH, M.; BEN-GAL, A. An artificial capillary barrier to improve root zone conditions for horticultural crops: Physical effects on water content. **Irrigation Science**, v. 29, n. 2, p. 171–180, 2011.

ITYEL, E.; LAZAROVITCH, N.; SILBERBUSH, M.; BEN-GAL, A. An artificial capillary barrier to improve root-zone conditions for horticultural crops: Response of pepper, lettuce, melon, and tomato. **Irrigation Science**, v. 30, n. 4, p. 293–301, 2012.

JEMCOV, I.; PETRIC, M. Measured precipitation vs. effective infiltration and their influence on the assessment of karst systems based on results of the time series analysis. **Journal of Hydrology**, v. 379, n. 3–4, p. 304–314, 2009.

KOOL, J.; PARKER, J. Development and evaluation of a closed form expressions for hysteretic soil hydraulic properties. **Water Resources Research**, v. 23, n. 1, p. 105–

114, 1987.

KRISDANI, H.; RAHARDJO, H.; LEONG, E.-C. Measurement of geotextile-water characteristic curve using capillary rise principle. **Geosynthetics International**, v. 15, n. 2, p. 86–94, 2008.

LI, J. H.; DU, L.; CHEN, R.; ZHANG, L. M. Numerical investigation of the performance of covers with capillary barrier effects in South China. **Computers and Geotechnics**, v. 48, p. 304–315, 2013.

LIMA, M. J.; AZEVEDO, M. M.; ZORNBERG, J. G.; PALMEIRA, E. M. Capillary barriers incorporating non-woven geotextiles. **Environmental Geotechnics**, v. 5, n. 3, p. 168–175, 2018.

LUNA, M.; ARCOS, D.; DURO, L. **Effects of grouting, shotcreting and concrete leachates on backfill geochemistry**. Stockholm, Sweden, 2006.

MAVROULIDOU, M.; GUNN, M. . Numerical modelling of flow in variably saturated porous media with fluctuating shallow water tables. Springer Proceedings in Physics 113, vol 113. **Anais...** , 2007.

MCCARTNEY, J. S.; ZORNBERG, J. G. Effects of infiltration and evaporation on geosynthetic capillary barrier performance. **Canadian Geotechnical Journal**, v. 47, n. 11, p. 1201–1213, 2010.

MELCHIOR, S. In-situ studies on the performance of landfill caps (Compacted soil liners, Geomembranes, Geosynthetic Clay Liners, Capillary Barriers). International Containment Technology Conference. **Anais...** . p.365–373, 1997.

MISZKOWSKA, A.; LENART, S.; KODA, E. Changes of permeability of nonwoven geotextiles due to clogging and cyclic water flow in laboratory conditions. **Water**, v. 9, n. 9, 2017.

MITCHELL, J. K.; ZORNBERG, J. G. Reinforced Soil Structures with Poorly Draining Backfills. Part II: Case Histories and Applications. **Geosynthetics International**, v. 2, n. 1, p. 265–307, 1995.

MORRIS, C. E.; STORMONT, J. C. Capillary barriers and subtitle D covers: estimating equivalency. **Journal of Environmental Engineering**, v. 123, n. 1, p. 3–10, 1997.

MORRIS, C. E.; STORMONT, J. C. Parametric Study of Unsaturated Drainage Layers in a Capillary Barrier. **Journal of Geotechnical and Geoenvironmental Engineering**, v. 125, n. 12, p. 1057–1065, 1999.

MUALEM, Y. A new model for predicting the hydraulic conductivity of unsaturated porous media. **Water Resources Research**, v. 12, n. 3, p. 513–522, 1976.

NCMA. **Segmental Retaining Walls Best Practices Guide**. 2016.

NG, C. W. W.; LIU, J.; CHEN, R.; XU, J. Physical and numerical modeling of an inclined three-layer (silt/gravelly sand/clay) capillary barrier cover system under extreme rainfall. **Waste Management**, v. 38, n. 1, p. 210–221, 2015.

PALMEIRA, E. M.; GARDONI, M. G. The Influence of Partial Clogging and Pressure on The Behaviour of Geotextiles in Drainage Systems. **Geosynthetics International**, v. 7, n. 4–6, p. 403–431, 2000.

PORTELINHA, F. H. M.; BUENO, B. S.; ZORNBERG, J. G. Performance of nonwoven geotextile-reinforced walls under wetting conditions: laboratory and field investigations. **Geosynthetics International**, v. 20, n. 2, p. 90–104, 2013.

PORTELINHA, F. H. M.; ZORNBERG, J. G. Effect of infiltration on the performance of an unsaturated geotextile-reinforced soil wall. **Geotextiles and Geomembranes**, v. 45, n. 3, p. 211–226, 2017.

PORTELINHA, F. H. M.; ZORNBERG, J. G.; PIMENTEL, V. Field performance of retaining walls reinforced with woven and nonwoven geotextiles. **Geosynthetics International**, v. 21, n. 4, p. 270–284, 2014.

RAHARDJO, H.; SATYANAGA, A.; HARNAS, F. R.; LEONG, E. C. Use of Dual Capillary Barrier as Cover System for a Sanitary Landfill in Singapore. **Indian Geotechnical Journal**, v. 46, n. 3, p. 228–238, 2016.

RAISINGHANI, D. V.; VISWANADHAM, B. V. S. Evaluation of permeability characteristics of a geosynthetic-reinforced soil through laboratory tests. **Geotextiles and Geomembranes**, v. 28, n. 6, p. 579–588, 2010.

RIANNA, G.; PAGANO, L.; URCIUOLI, G. Investigation of soil-atmosphere interaction in pyroclastic soils. **Journal of Hydrology**, v. 510, p. 480–492, 2014.

RICHARDS, L. A. Capillary conduction of liquids through porous mediums. **Physics**, v. 1, p. 318–333, 1931.

ROSSI, M.; DONNINI, M. Estimation of regional scale effective infiltration using an open source hydrogeological balance model and free/open data. **Environmental Modelling and Software**, v. 104, p. 153–170, 2018.

ROY, D. M. Relationships between permeability, porosity, diffusion and microstructure of cement pastes, mortar, and concrete at different temperatures. Symposium P - Pore structures and permeability of cementitious materials. **Anais...** v. 137, p.179–189, 1989.

SIEMENS, G.; BATHURST, R. J. Numerical parametric investigation of infiltration in one-dimensional sand-geotextile columns. **Geotextiles and Geomembranes**, v. 28, n. 5, p. 460–474, 2010.

STORMONT, J. C.; MORRIS, C. E. Characterization of Unsaturated Nonwoven Geotextiles. *Advances in Unsaturated Geotechnics*. **Anais...** p.153–164, 2000.

STORMONT, J. C.; RAMOS, R.; HENRY, K. S. Geocomposite capillary barrier drain system with fiberglass transport layer. **Transportation Research Record: Journal of the Transportation Research Board**, v. 1772, n. 1, p. 131–136, 2001.

TAKE, W. A.; BOLTON, M. D. Seasonal ratcheting and softening in clay slopes, leading to first-time failure. **Géotechnique**, v. 61, n. 9, p. 757–769, 2011.

TAMI, D.; RAHARDJO, H. Characteristics of scanning curves of two soils. **Soils and Foundations**, v. 47, n. 1, p. 97–108, 2007.

TAN, S. A.; CHEW, S. H.; NG, C. C.; et al. Large-scale drainage behaviour of composite geotextile and geogrid in residual soil. **Geotextiles and Geomembranes**, v. 19, n. 3, p. 163–176, 2001.

TATSUOKA, F.; YAMAUCHI, H. A reinforcing method for steep clay slopes using a non-woven geotextile. **Geotextiles and Geomembranes**, v. 4, n. 3–4, p. 241–268, 1986.

THUO, J. N.; HUYNH, V. D. A.; YANG, K.; PORTELINHA, F. H. M. Behavior of Geotextile / Geogrid Reinforced Slopes with Various Backfills subject to Rainfalls. 6th Asian Regional Conference on Geosynthetics. **Anais...** . p.1–10, 2016.

THUO, J. N.; YANG, K.-H. Numerical study of infiltration into unsaturated clay slopes with nonwoven geotextile drains sandwiched in sand cushions: Featuring the capillary barrier effect. **10th International Conference on Geosynthetics, ICG 2014**, , n. 2004, 2014.

THUO, J. N.; YANG, K. H.; HUANG, C. C. Infiltration into unsaturated reinforced slopes with nonwoven geotextile drains sandwiched in sand layers. **Geosynthetics International**, v. 22, n. 6, p. 457–474, 2015.

VAHEDIFARD, F.; MORTEZAEI, K.; LESHCHINSKY, B. A.; LESHCHINSKY, D.; LU, N. Role of suction stress on service state behavior of geosynthetic-reinforced soil structures. **Transportation Geotechnics**, v. 8, p. 45–56, 2016.

VANAPALLI, S. K.; FREDLUND, D. G.; PUF AHL, D. E.; CLIFTON, A. W. Model for the prediction of shear strength with respect to soil suction. **Canadian Geotechnical Journal**, v. 33, p. 379–392, 1996.

WILSON, G. W.; FREDLUND, D. G.; BARBOUR, S. L. The effect of soil suction on evaporative fluxes from soil surfaces. **Canadian Geotechnical Journal**, v. 34, n. 1, p. 145–155, 1997.

YANG, K.-H.; THUO, J. N.; HUYNH, V. D. A.; NGUYEN, T. S.; PORTELINHA, F. H. M. Numerical evaluation of reinforced slopes with various backfill-reinforcement-drainage systems subject to rainfall infiltration. **Computers and Geotechnics**, v. 96, n. June, p. 25–39, 2018.

YANG, K. H.; UZUOKA, R.; THUO, J. N. ANG A; LIN, G. L.; NAKAI, Y. Coupled hydro-mechanical analysis of two unstable unsaturated slopes subject to rainfall

infiltration. **Engineering Geology**, v. 216, p. 13–30, 2017.

YVONNE LINS, YAZHOU ZOU, T. Physical Modeling of SWCC for Granular Materials. Springer Proceedings in Physics. **Anais...** . p.61–74, 2013.

ZHAN, T. L. T.; LI, H.; JIA, G. W.; CHEN, Y. M.; FREDLUND, D. G. Physical and numerical study of lateral diversion by three-layer inclined capillary barrier covers under humid climatic conditions. **Canadian Geotechnical Journal**, v. 51, n. 12, p. 1438–1448, 2014.

ZORNBERG, J. G.; BOUAZZA, A.; MCCARTNEY, J. S. Geosynthetic capillary barriers: Current state of knowledge. **Geosynthetics International**, v. 17, n. 5, p. 273–300, 2010.

ZORNBERG, J. G.; MITCHELL, J. K. Reinforced Soil Structures with Poorly Draining Backfills. Part I: Reinforcement Interactions and Functions. **Geosynthetics International**, v. 1, n. 2, p. 103–148, 1994.